Chapter 9

Performance

9.1 Overview

In order to assess the basic performance of the CMS Phase I and II Trackers we discuss a series of increasingly challenging physics problems using the simulation and reconstruction tools introduced in Chapters 7 and 8.

The algorithms employed to generate single track, minimum bias, di-jet and B-meson-decay events are discussed in Section 9.2. The high luminosity LHC conditions are simulated overlaying the pile-up events described in Section 7.11 on the hard interactions under study.

Single track events are used in Section 9.3 to evaluate the precision of track measurement in the CMS inner detector. Good momentum resolution is essential for the mass determination and background suppression for particles with small natural width. The transverse momentum of the decay products ranges from the very low values typical of B-physics up to a few TeV in the case of new heavy bosons. Accurate momentum measurements are also necessary to calibrate the EM calorimeter. High efficiency of charge determination for tracks up to several TeV is needed to maintain good heavy boson reconstruction efficiency in the kinematic range accessed by the LHC. The probability of charge mis-assignment is studied using single muons of transverse momentum as high as 4 TeV. The track impact parameter resolution, relevant to b-jet identification and lifetime measurements, is studied for muons and pions at several p_T values; the deviation of the momentum and impact parameter resolution from a Gaussian behaviour are discussed for low p_T muons and hadrons, due to their importance in b-jets identification and exclusive B-decays reconstruction.

The efficiency for correctly reconstructing single tracks is analysed separately for muons and hadrons and a possible degradation due to the larger occupancy expected at the high luminosity LHC condition is studied using the Phase II CMS Tracker layout. To limit the impact of the Tracker material budget, dedicated procedures were developed to reconstruct electrons and hadrons, discussed in Section 9.4.

Isolated leptons and photons are a clean signature of bosons and SUSY particles; isolation criteria are effective to suppress jet background and rely on the ability to reconstruct low p_T tracks with high efficiency within jets. Moreover, good track finding efficiency in jets associated to precise measurement of the track impact parameter allows the identification of b-jets. The ability to reconstruct tracks in jets is discussed in Section 9.5 as a function of the jet E_T and at different luminosity conditions whereas b-jet identification with the CMS Tracker is discussed in Section 9.7. Tagging b-jets of high transverse energy is a fundamental tool for Higgs and SUSY particle searches; the expected b-jet transverse energy varies typically between few tens of GeV and 200 GeV for the hardest events; the b-tagging capability of the CMS Tracker is studied as a function of jet E_T and both at low and high luminosity. The identification of heavy flavour secondary vertices is also potentially a powerful tool to tag b-jets and is discussed in

Section 9.6 together with a more general strategy of vertex reconstruction. The primary vertex reconstruction efficiency depends on the vertex topology and good track measurement typically ensures satisfactory performance of relatively simple algorithms. A challenging task is set by the reconstruction of V_0 vertices, needed to identify K_s^0 and access the CP violation sector. This problem is addressed by a study of the $B_d^0 \to J/\psi K_s^0$ reaction. Special attention is given to the reconstruction of photon conversions, which are a large source of background in primary lepton identification. Conversions reconstruction increases the detection efficiency of $H \to \gamma\gamma$ events; moreover a precise reconstruction of the parent photons can be used to localise the reaction vertex in high luminosity events.

In addition to pp operation, the LHC will be able to collide heavy ions, such as lead, calcium and nickel. In a typical running schedule three to four weeks per year will be dedicated to ion collisions. The suppressed production of heavy-quark bound states is a signature to study a Quark-Gluon Plasma state of hadronic matter. The most demanding measurements concern Pb-Pb collisions, that have a centre-of-mass energy of 5.5 TeV per nucleon-nucleon pair and the highest track multiplicity. A study of identification of Υ's produced in Pb-Pb collisions in the CMS detector is reported in Section 9.8. In the following we shall designate the detector consisting of the low luminosity Pixel detector configuration and the staged silicon and MSGC Trackers as the Phase I detector layout. The fully instrumented strip detector combined with the high luminosity version of the Pixels will be referred to as Phase II Tracker.

9.2 Physics Simulation

9.2.1 Single tracks

The single track generator allows the user to choose the identity of particles to be generated as well as kinematic ranges in pseudorapidity η, azimuth angle ϕ and transverse momentum p_T. By default the distributions in η and ϕ are uniform in a user defined range. Two options are available for p_T sampling: 1) realistic p_T distribution whose asymptotic behaviour is ${p_T}^{-\alpha}$ ($\alpha = 3.78$) or 2) flat distribution within a user defined interval.

The single particle generation option is used to study the Tracker single particle performance. An option is also available to generate hits by geantinos (artificial, neutral and non-interacting particles), which were used to estimate the fractional radiation and interaction lengths of the Tracker material.

9.2.2 Minimum bias events

Inelastic minimum bias events are generated using PYTHIA.[1] The pseudorapidity distributions of charged particles is shown in Fig. 9.1a for all p_T and for two different p_T cuts. The plot is normalised to the number of particles per pseudorapidity unit per pp event. In the central region the charged particle density is about seven per unit of pseudorapidity. Charged particles from weak decays, which are not included, would contribute about 10% to the plot. The mean number of non-spiralling particles ($p_T > 0.9$) is about one per pseudorapidity unit. The transverse momentum of charged particles is shown in Fig. 9.1b. The mean p_T is about 0.5 GeV/c and is almost independent of pseudorapidity in the region of the Tracker acceptance. The multiplicity of photons from pp collisions (mainly from π^0 decays) is about 8.3 per unit of rapidity. For high luminosity, $\mathcal{L} = 10^{34}$ cm^{-2}s^{-1}, the mean number of photons from the interaction point in one trigger is about 1000 in the range $|\eta| < 2.5$, assuming about 25 pp events per trigger on average.

[1] The PYTHIA switches were set at msel=1, mstp(2)=2, mstp(33)=3, mstp(81)=1 and mstp(82)=4

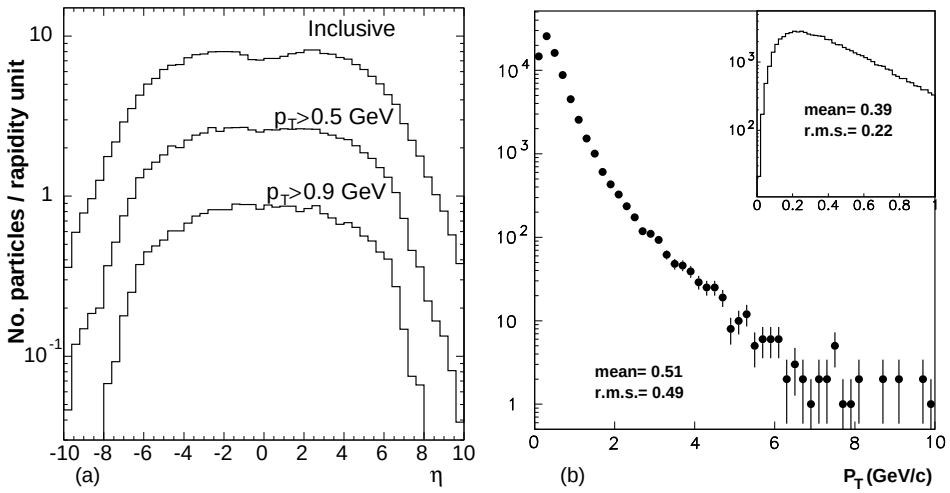

Fig. 9.1: a) Pseudorapidity of charged particles in MB events. b) Transverse momentum of charged particles in MB events.

9.2.3 B-meson decay events

The $B_d^0 \to J/\psi K_S^0 \to \mu\mu\pi\pi$ decay mode, a 'gold plated' channel in the study of CP violation, is chosen to illustrate the Tracker performance in reconstructing the kinematics of B-mesons decays. The accompanying $\bar{B}_d^0$ meson is required to decay semileptonically into a muon. The generation is performed using the $b\bar{b}$ event simulation package [9-1], based on PYTHIA. The sample contains the proper mixture of events generated by gluon fusion and by gluon splitting. All decay products are required to be within the region $|\eta| \leq 2.4$ and only pions with $p_T \geq 0.5$ GeV/c are selected.

The muons produced from the J/ψ decay are required to reach at least two muon stations in order to be identified. To tag the flavour of the accompanying meson, the highest p_T muon not originating from the J/ψ decay is used. To prevent the trigger from introducing artificial charge asymmetry, the tagging muon must reach two muons stations in a region where the detector acceptance and the triggering probability are equal for positive and negative muons. Of the three muons considered, at least two are required to satisfy the trigger requirements. Approximately 3700 events, corresponding to 0.5% of the initial sample, are selected. The total number of $B_d^0 \to J/\psi K_S^0 \to \mu\mu\pi\pi$ events per year satisfying these criteria is expected to be ~32000 at $\mathcal{L}$=10^{33} cm^{-2}s^{-1}. Figure 9.2 illustrates the kinematics of the particles to be reconstructed.

9.2.4 Di-jet events

To evaluate the Tracker performance for charged tracks within high p_T jets, several samples of $u\bar{u}$ events with jet E_T ranging from 20 GeV to 200 GeV were generated in the pseudorapidity interval $|\eta| \leq 2.5$. To study the b-tagging efficiency, $b\bar{b}$ events with jets of diverse E_T and η are used. We required explicitly that the b quark be contained in the jet cone, neglecting in this way the model-dependent inefficiency due to hard gluon emission that may occur during the b quark evolution. The b-tagging fake rate is studied using $u\bar{u}$ events. To estimate the intrinsic capability to reject fake tags, we use the subset of events that do not contain b or c quarks generated by gluon splitting. Jets are clustered in cones of radius $R = \sqrt{\Delta\eta^2 + \Delta\phi^2} = 0.4$ by the PYTHIA routine LUCELL, using exclusively the Monte Carlo generator information. The charged track multiplicity within jets as a function of jet E_T is shown in Fig. 9.3 for tracks of any p_T (closed dots) and for tracks with $p_T \geq 0.9$ GeV/c (dashed line). The transverse momentum

of charged tracks within the jet cones is shown in Fig. 9.4 in which only tracks with p_T larger than 0.9 GeV/c are considered.

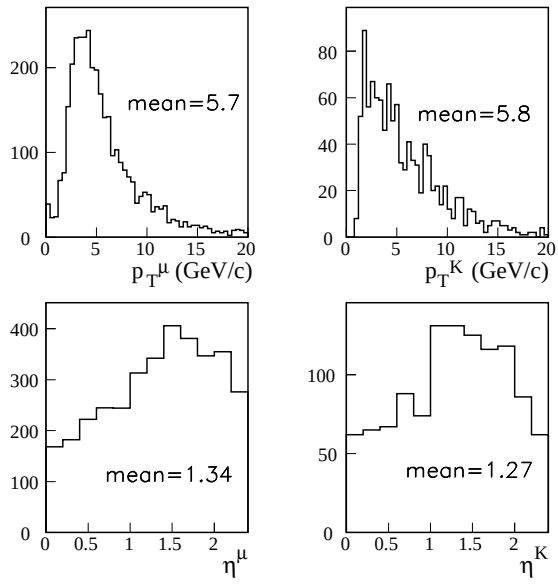

Fig. 9.2: Kinematic properties of the K_S^0 and of the muons produced by the J/ψ and $\bar{B}_d^0$ decays.

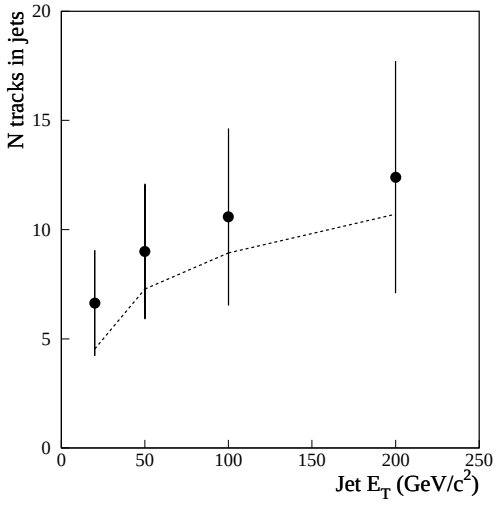

Fig. 9.3: Charged particle multiplicity in jets as a function of jet E_T.

9.3 Single Track Performance

A reconstructed track is described in the CMS convention by six parameters: x_{imp}, y_{imp}, z_{imp}, ϕ_0, c and $\cot\theta$. The quantities x_{imp}, y_{imp}, z_{imp} measure the coordinates of the impact point, i.e. the point on the track trajectory set at the distance of closest approach to the nominal vertex (0,0), measured in the transverse plane. The azimuthal angle of the tangent to the track at the impact point, ϕ_0, and $\cot\theta$ measure the pointing direction of the track, with θ the track polar angle. The signed curvature c is expressed by $B_z q/p_T$, where B_z is the longitudinal component

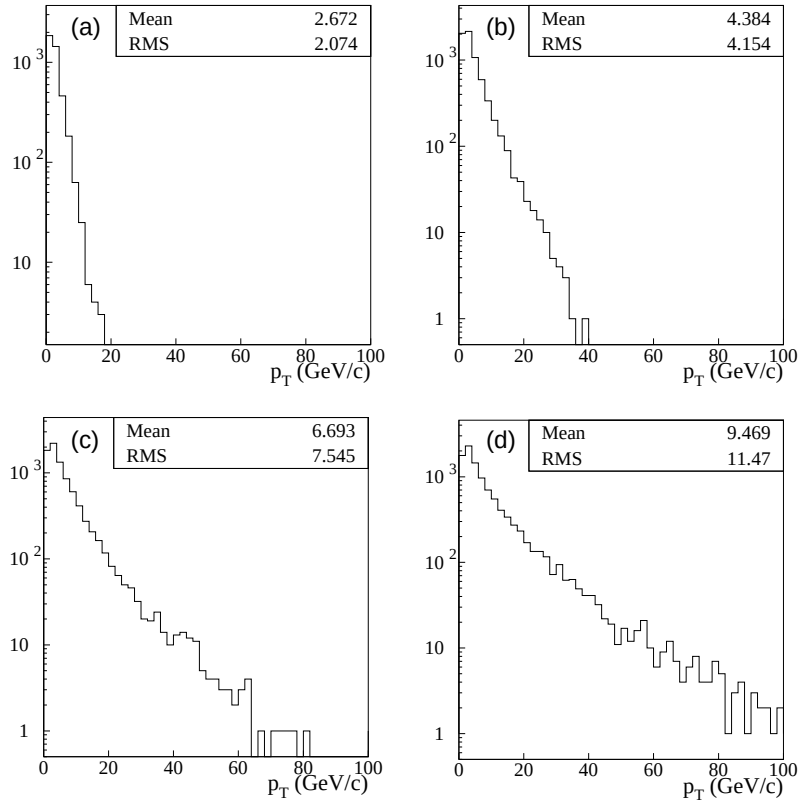

Fig. 9.4: Transverse momentum of tracks in jets of a) 20 GeV E_T b) 50 GeV E_T, c) 100 GeV E_T and d) 200 GeV E_T. All tracks have $p_T \geq$0.9 GeV/c and are within R=0.4 from the jet axis.

of the magnetic field, q and p_T are the particle charge and transverse momentum. The accuracy of the track parameter measurement is estimated using muons of several p_T values. Tracks are reconstructed using the Global Track Finder algorithm (GTF); a comparison between the performance of GTF and the Connection Machine algorithm (CM) is briefly discussed in the next section.

9.3.1 Impact parameter resolution

We define the transverse impact parameter as $d_0 = y_{imp}\cos\phi_0 - x_{imp}\sin\phi_0$. The precision of the impact point measurement is dominated by the Pixel hit position resolution and affected by multiple scattering in the innermost Pixel layer. The d_0 resolution is shown in Fig. 9.5 for the Phase I Tracker layout. We define the d_0 resolution as the difference of the reconstructed and generated parameters and we neglect any deterioration due to misalignment. The track origin is smeared according to the expected Gaussian fluctuations ($\sigma_x = \sigma_y = 15$ μm and $\sigma_z = 5.3$ cm). For high p_T tracks, the accuracy is dominated by the precision of the measurement in the innermost Pixel layer, located at a distance of 4 cm from the beam line; the resolution is independent of η and is about 9 μm. The d_0 resolution is limited by multiple scattering when the track transverse momentum is smaller than 10 GeV/c; the visible degradation at large pseudorapidity reflects the increase of the material traversed by the tracks. In the Phase II layout, the innermost Pixel layer is set at a larger radius (7 cm) and the estimated asymptotic resolution is 12 μm, as shown in Fig. 9.6.

The z_{imp} resolution is shown in Fig. 9.7 for the Phase I Tracker. At low momenta, the presence of multiple scattering degrades the z_{imp} resolution and a strong dependence on $|\eta|$ is

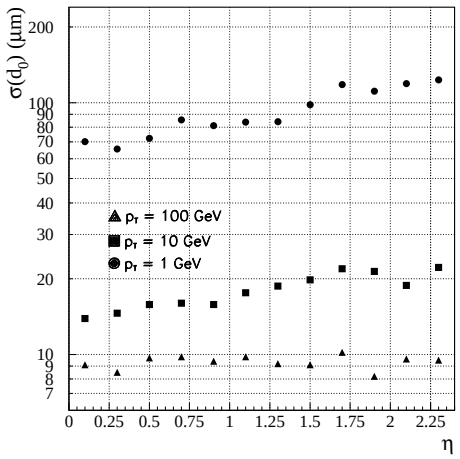

Fig. 9.5: d_0 resolution as a function of η for muons of several p_T values. Phase I CMS Tracker Layout.

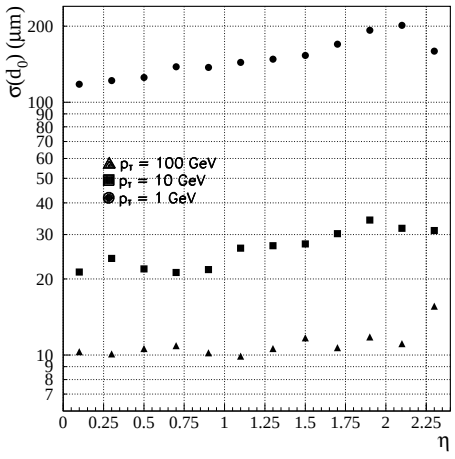

Fig. 9.6: d_0 resolution as a function of η for muons of several p_T values. Phase II CMS Tracker Layout.

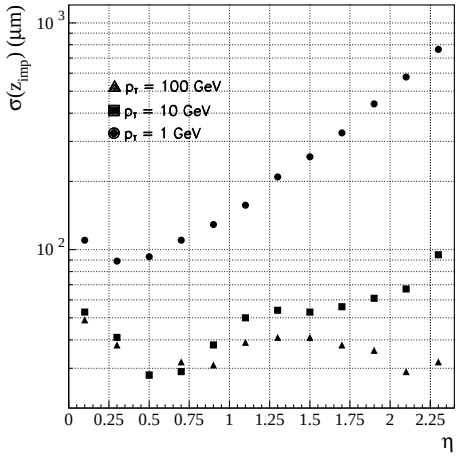

Fig. 9.7: z_{imp} resolution as a function of η, for muons of p_T =1, 10 and 100 GeV/c. Phase I CMS Tracker Layout.

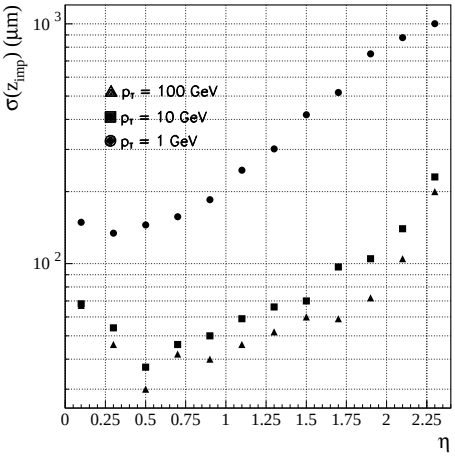

Fig. 9.8: z_{imp} resolution as a function of η, for muons of p_T =1, 10 and 100 GeV/c. Phase II CMS Tracker Layout.

observed. When high p_T muons are measured by the Pixel barrel, the z_{imp} resolution can be approximated by $\sigma_z \sqrt{r_1^2 + r_2^2}/(r_2 - r_1)$, where σ_z is the Pixel hit resolution and r_1, r_2 represent the radii of the Pixel barrel layers. This expression is calculated assuming that the impact parameter is measured using information from only the two Pixel layers. The hit z-resolution varies as a function of η and the cluster size yields the best resolution at $\eta \sim 0.5$. At large η, a degradation of the Phase II detector performance is observed with respect to the Phase I Tracker. In Phase I the innermost Pixel layer extends up to $|\eta| = 2.3$ whereas in the Phase II Tracker the z_{imp} measurement at large pseudorapidity ($|\eta| \geq 2$) is provided exclusively by the

Pixel endcaps. In the forward detectors, which measure the radial position with precision σ_r, the z_{imp} resolution depends on η as $\sigma_r \cot\theta$, as shown in Fig. 9.8 for high p_T tracks.

The comparison between the d_0 resolution estimated by two different pattern recognition algorithms, GTF and CM, is shown in Fig. 9.9. High p_T muons are used in order to disentangle the intrinsic hit precision and fitting performance from multiple scattering effects. Since no significant differences are observed between the two algorithms, only the GTF performance is described in the rest of this section.

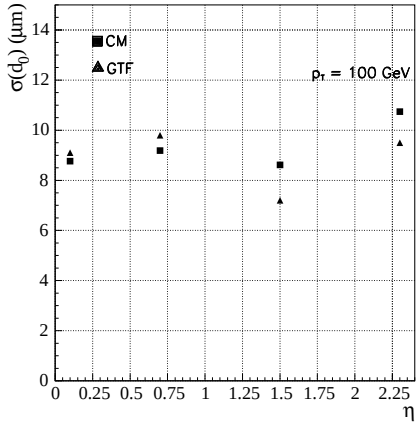

Fig. 9.9: d_0 resolution measured using the two track reconstruction algorithms, GTF and CM. Phase I Tracker layout.

9.3.2 Transverse momentum resolution

The precision of the track curvature measurement is discussed here in terms of $\sigma(p_T)/p_T$. Fig. 9.10 shows the transverse momentum resolution as a function of η for muons traversing the Phase I Tracker. No beam constraint is imposed during the fitting procedure. The momentum resolution for high p_T tracks ($\sim$ 100 GeV/c) has a modest dependence on pseudorapidity in the interval $|\eta| \leq 1.7$, in which we measure $\sigma_{p_T}/p_T \sim$ 1-2%. At larger $|\eta|$ the resolution worsens as the Tracker lever arm decreases. For lower p_T tracks, multiple scattering becomes significant and induces an η-dependence on the momentum resolution, reflecting the amount of material traversed by the tracks. The Phase II and Phase I detectors perform equally well, as can be observed by comparing Figs. 9.10 and 9.11.

9.3.3 Angular resolution

The ϕ_0 resolution measured with the Phase I and Phase II tracking detectors is shown in Figs. 9.12 and 9.13, respectively; it is fairly independent of η due to the constant number of precision hits over the full pseudorapidity range. The $\cot\theta$ resolution is shown in Figs. 9.14 and 9.15 for the two Tracker layouts. The accuracy of the measurement is dominated by the Pixel detector and the behaviour as a function of p_T and η is the same as for z_{imp}, discussed in Section 9.3.1.

9.3.4 Track finding efficiency

The efficiency to reconstruct single muon tracks in the Phase I detector is estimated using GTF. A track is defined to be successfully reconstructed if it shares more than 50% of the hits with the generated helix. Reconstructed tracks are required to have at least six hits. The Tracker is fully efficient for energetic muons in the whole pseudorapidity range, as shown in Fig. 9.16a.

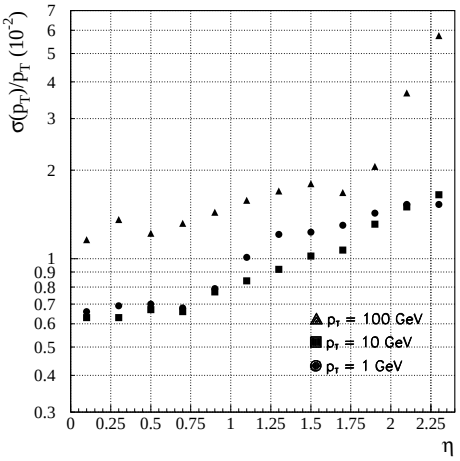

Fig. 9.10: Transverse momentum resolution as a function of η for muons of several p_T values. Phase I Tracker layout.

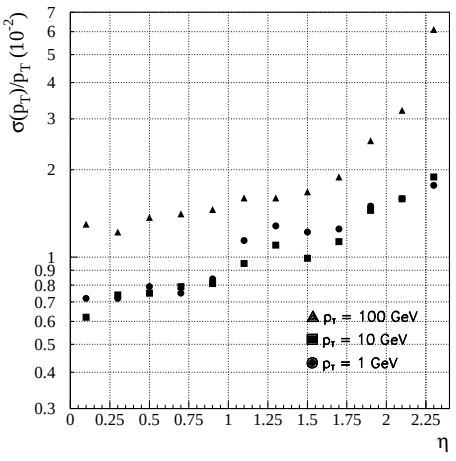

Fig. 9.11: Transverse momentum resolution as a function of η for muons of several p_T values. Phase II Tracker layout.

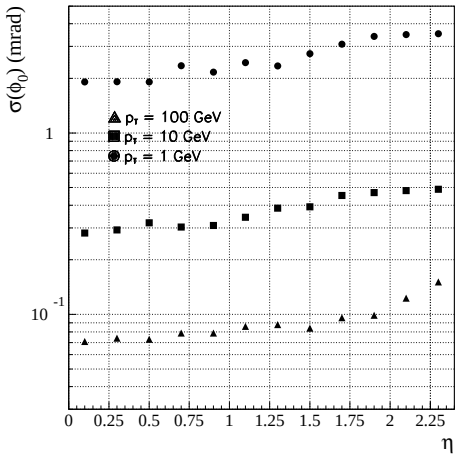

Fig. 9.12: ϕ_0 resolution as a function of η for muons of several p_T values. Phase I CMS Tracker Layout.

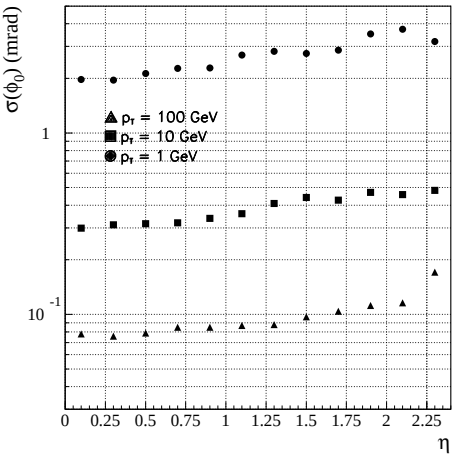

Fig. 9.13: ϕ_0 resolution as a function of η for muons of several p_T values. Phase II CMS Tracker Layout.

A drop in efficiency of about 2% is observed for muons of $p_T = 1$ GeV/c in the region around $\eta = 1$, due to the gap between the barrel and endcap MSGC detectors. In this region the hermeticity of the MSGC Tracker deteriorates slightly and low p_T tracks are affected by the additional reduction of hit reconstruction efficiency due to cluster splitting (Fig. 7.55). GTF makes use of backward propagation and therefore is slightly penalised by the lack of outer hits to seed the track as well as by the occasional loss of two subsequent hits. Moreover, a sizeable amount of material is present in the barrel-endcap transition region, contributed by the barrel services and end-flanges.

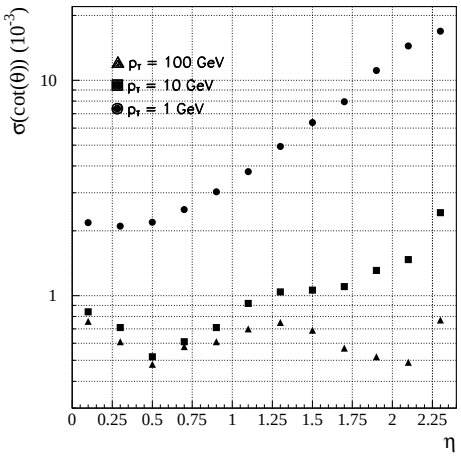

Fig. 9.14: $\cot\theta$ resolution as a function of η, for muons of several p_T values. Phase I CMS Tracker Layout.

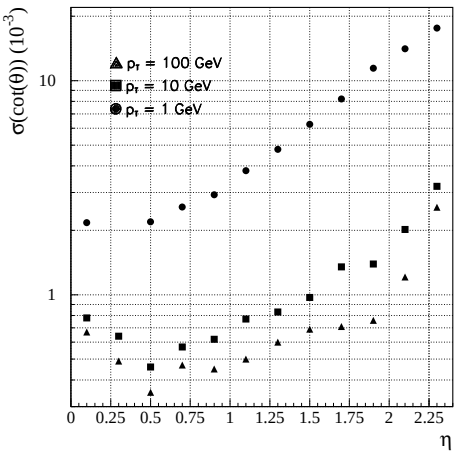

Fig. 9.15: $\cot\theta$ resolution as a function of η, for muons of several p_T values. Phase II CMS Tracker Layout.

In Fig. 9.16b a tighter definition of efficiency is used: a track is considered as properly reconstructed if all of the parameters of the fitted helix differ from the true value by less than five times the fitted error. The efficiency remains very high, which demonstrates the good quality of the fit.

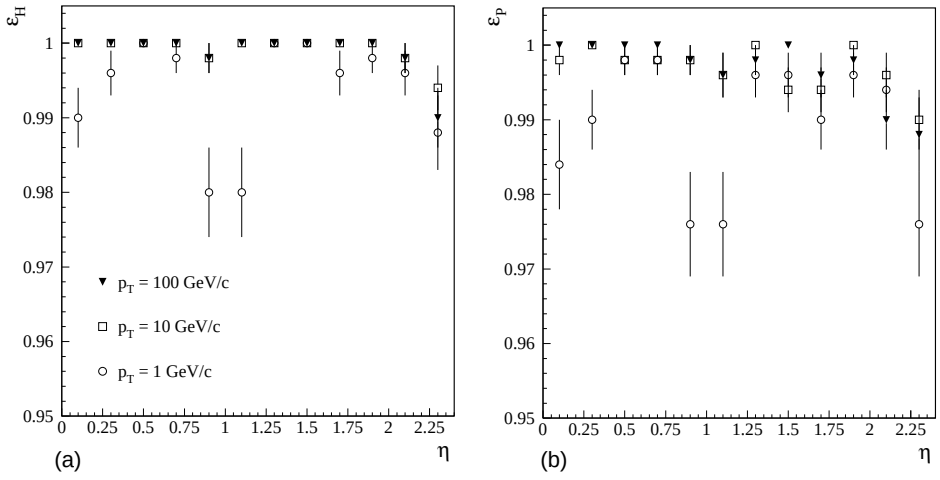

Fig. 9.16: Track finding efficiency for single muons as a function of pseudorapidity, for three different values of the transverse momentum. In (a) the efficiency is defined on the basis of the number of correct hits associated to the fitted track. In (b) a tighter criterion is applied, based on the quality of the fit, as explained in the text.

9.3.5 Charge assignment efficiency

The strong magnetic field in which the Tracker operates provides an excellent charge determination capability. The charge mis-assignment probability is estimated as a function of pseudo-

rapidity for muon tracks of transverse momentum between 1 and 4 TeV/c. Results are shown in Fig. 9.17.

The functional dependence on the pseudorapidity is directly related to the behaviour observed for the momentum resolution. The increase around $\eta = 1$ is due to the gap between the MSGC barrel and endcap. The marked increase at $\eta > 1.7$ is due to the lever arm reduction at the end of the MSGC endcap.

The charge mis-assignment probability for tracks of $p_T = 1$ TeV/c is about 10^{-4} in the barrel region and increases up to 0.5% at the largest pseudorapidity. In the barrel, the charge of tracks with $p_T = 4$ TeV/c is reconstructed with a mis-assignment probability of a few percent.

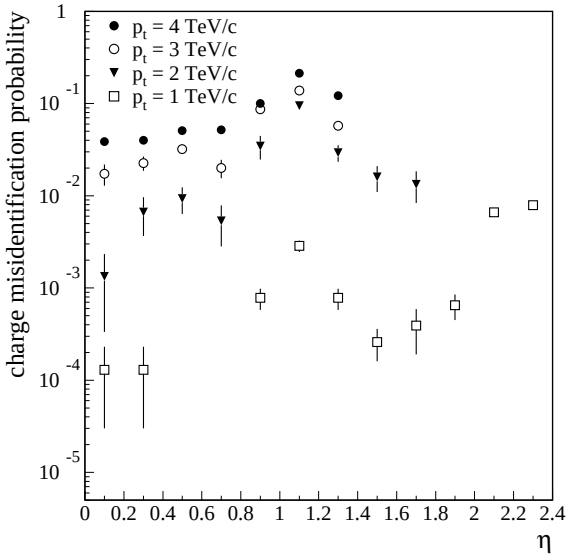

Fig. 9.17: Charge misidentification probability for high p_T tracks as a function of pseudorapidity.

9.3.6 Tails of distributions

The quality of track reconstruction can be studied by analysing the *pull* distributions of the estimated parameters. Pull distributions are defined here as the difference between the reconstructed and generated parameters, normalised to the error on the fitted parameter. A pull distribution of the $1/p_T$ variable, obtained for 10 GeV/c muons at $\eta \leq 0.2$, is shown in Fig. 9.18. The distribution has $\sigma = 1.01$. In order to investigate deviations from a Gaussian behaviour, a study of the pull tails was performed. The 'tail fraction' is defined as the fraction of the pull population satisfying the condition

$$\frac{|P_{reconstructed} - P_{generated}|}{\sigma_P} \geq 3\,\sigma_{pull}$$

where P is a track parameter, σ_P its error and σ_{pull} is obtained from a Gaussian fit of the core of the pull in different η intervals. For this study, the Phase II Tracker layout has been used. The x_{imp} and $1/p_T$ tail fractions are studied for low p_T muons in the pseudorapidity range $0 \leq \eta \leq 2.4$; the robustness of the track reconstruction procedure is evaluated using diverse requirements on the number and type of hits used to fit the track. Tracks with two reconstructed Pixel hits are better measured, as shown in Figs. 9.19 and 9.20. Figures 9.21 and 9.22 show the tail fractions for 1 GeV/c p_T muons, reconstructed requiring a minimum of six hits per track. A comparison is shown with the tail fraction associated to the standard requirement of eight hits per track; the tail fractions are compatible within errors. Two Pixel hits are explicitly required

in both cases. The tail fractions are larger than the value expected for a Gaussian statistics (0.27%). The deviations are partially accounted for by large multiple scattering effects and by the imperfect description of the Tracker material used in the track propagation procedure; in fact, the track reconstruction algorithm uses a simplified geometry model in which the detailed variation of material density in the detector is neglected. As mentioned in the discussion of the track finding efficiency, part of the performance deterioration is also due to badly reconstructed clusters.

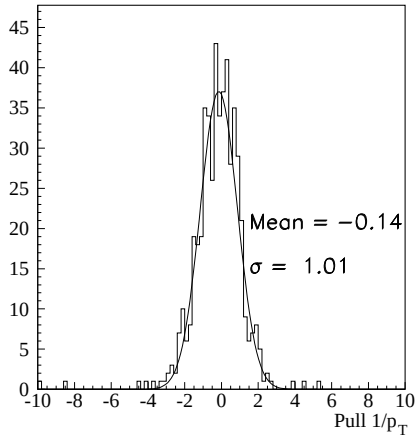

Fig. 9.18: Pull of the $1/p_T$ variable, for 10 GeV/c p_T muons at $\eta \leq 0.2$.

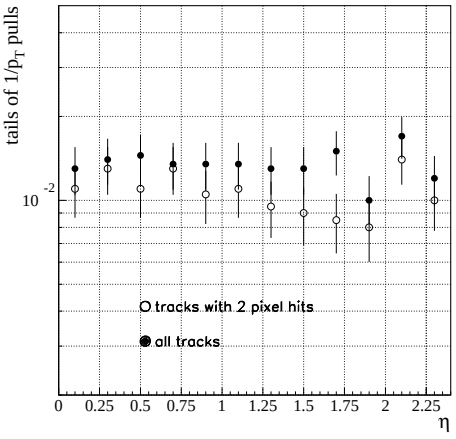

Fig. 9.19: Tail fraction for $1/p_T$ pull as a function of η for 10 GeV/c p_T muons; an explicit requirement of two Pixel hits per track is compared to the standard reconstruction procedure.

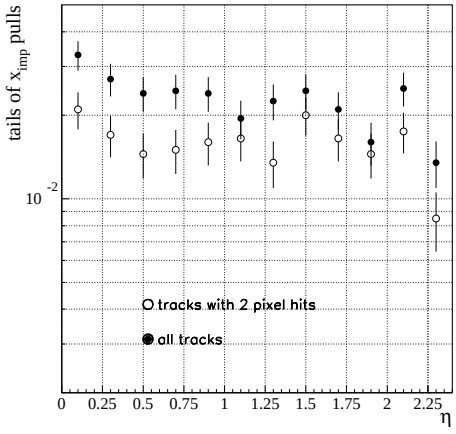

Fig. 9.20: Tail fraction of impact parameter pull as a function of η for 10 GeV/c p_T muons; an explicit requirement of two Pixel hits per track is compared to the standard reconstruction procedure.

9.3.7 Effect of pile-up

The pile-up minimum bias events generate a large number of hits in the CMS Tracker and can affect the track finding efficiency and the fit accuracy. The efficiency to reconstruct p_T =

10 GeV/c muons as a function of pseudorapidity is shown in Fig 9.23. Reconstructed tracks are required to share at least 50% of their hits with the parent helix and to have more than five or 'at least six' reconstructed clusters in the Tracker. The study is performed using GTF. The efficiency is estimated using the Phase II Tracker layout in high luminosity conditions. The track finding efficiency in absence of pile-up is also shown for comparison. No degradation of the performance is observed in the central region of the detector, whereas a loss of 1-2% is noticeable for pseudorapidities $|\eta| > 1$. A study of the tail fractions of the transverse momentum and transverse impact parameter pulls of 10 GeV/c muons is shown in Figs. 9.24. For these tracks we require two Pixel hits. The deviations from Gaussian behaviour of the $1/p_T$ and x_{imp} pulls are unaffected by the presence of pile-up events.

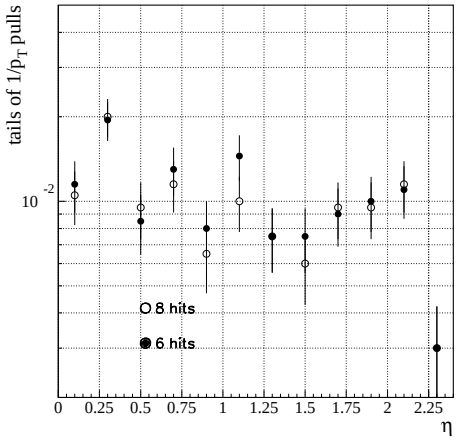

Fig. 9.21: Tail fraction for $1/p_T$ pull as a function of η for 1 GeV/c p_T muons; two different requirements are imposed on the minimum number of reconstructed hits per track. Two Pixel hits are explicitly required in both cases.

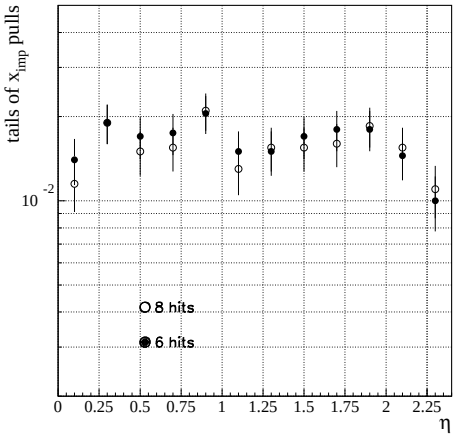

Fig. 9.22: Tail fraction for transverse impact parameter pull as a function of η for 1 GeV/c p_T muons; two different requirements are imposed on the minimum number of reconstructed hits per track. Two Pixel hits are explicitly required in both cases.

9.4 Isolated Tracks

9.4.1 Electron reconstruction

Electrons traversing the Tracker lose energy by bremsstrahlung: on average, the fraction of radiated energy is approximately 20% at $\eta \simeq 0$ and it increases up to 55% in the region where the amount of material is largest ($1.2 \leq |\eta| \leq 2.2$). Standard track reconstruction methods cannot handle sizeable variations of curvature along the track path, which may result either in low quality measurements of the track parameters or in the inability of the reconstruction procedure to identify a track candidate. The track reconstruction efficiency for electrons of 10 GeV/c and 40 GeV/c transverse momentum is shown in Fig. 9.25 as a function of pseudorapidity. Tracks are reconstructed with GTF; they are required to have more than seven hits and to share at least 50% of the hits with the parent track. The track finding efficiency is influenced by the amount of material in the Tracker. The fraction of energy lost by bremsstrahlung is estimated to be largely independent of the electron p_T and therefore low p_T tracks are penalised by larger curvature deviations in the 4 T magnetic field. The electron reconstruction efficiency and momentum

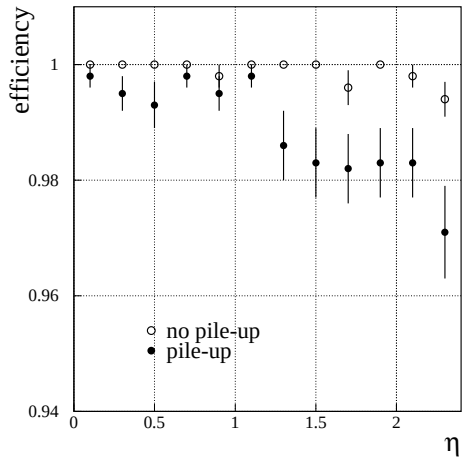

Fig. 9.23: Track finding efficiency for single muons of $p_T = 10$ GeV/c in high luminosity events. Phase II layout.

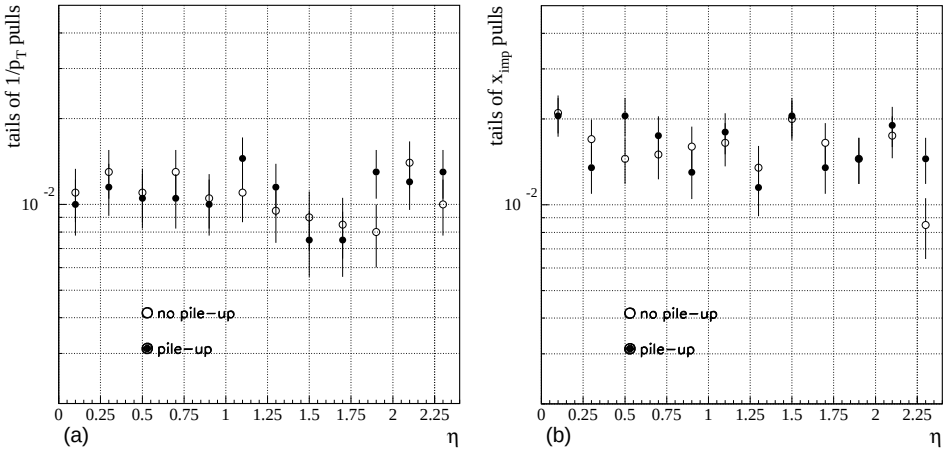

Fig. 9.24: Tail fraction for a) $1/p_T$ and b) x_{imp} pulls as a function of η for p_T =10 GeV/c muons, with and without pile-up. Phase II Tracker layout.

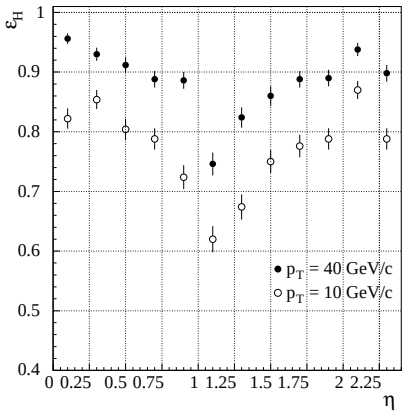

Fig. 9.25: Track finding efficiency for 10 GeV/c and 40 GeV/c p_T electrons as a function of pseudorapidity; tracks are reconstructed using GTF.

measurement can be improved by procedures recovering the effects of bremsstrahlung. In the study reported in the following, we estimate the impact of energy losses on the measurement of electrons in the CMS Tracker, and analyse the effect of a simple recovery procedure. The efficiency to reconstruct electrons of transverse momentum larger than 10 GeV/c becomes larger than 90% even in the η intervals where the Tracker material budget is largest.

9.4.1.1 Bremsstrahlung recovery method

The degradation of the electron momentum measurement due to bremsstrahlung can be partially recovered by using the estimate of the shower position in the EM calorimeter. The energy barycentre of the electron-photon shower is a good estimator of the impact point of the electron in absence of bremsstrahlung; in fact, the $r\phi$ distance between electron and photon is proportional to the fraction of the electron E_T taken by the photon. In this preliminary study, the reconstructed energy of the electromagnetic cluster is approximated by smearing the original electron energy; the position of the cluster barycentre is obtained by smearing the electron point of impact on the EM calorimeter, estimated in absence of bremsstrahlung. The resolutions we use are shown in Table 9.1. These values are obtained by scaling the resolutions estimated for photons in [1-2] by a conservative factor of about 3.5, that accounts for the possible degradation of performance in the complex scenario where the clusters of electron and photons have partial overlap.

Table 9.1: Calorimeter energy and ϕ resolution used in this study together with the expected p_T resolution of the re-fitted tracks; two electron transverse momenta and two pseudorapidity values are considered.

p_T (GeV/c)	η	σ_E (GeV)	σ_E/E (%)	σ_ϕ (mrad)	σ_{p_T}/p_T (%)
10	0.17-0.26	0.68	6.7	4.24	5
10	1.26-1.35	0.78	4.0	3.39	5
40	0.17-0.26	1.04	2.5	3.22	20
40	1.26-1.35	1.59	2.0	2.96	20

The recovery procedure begins by identifying badly reconstructed electrons. Clusters and tracks are associated by their position in the rz plane; the matching quality in the $r\phi$ plane is estimated by a χ^2 relying on the track and EM cluster information and on the E/p estimate[2]. For poorly matched tracks, the transverse momentum is recalculated using the shower barycentre, the beam constraint and the hit measured in the first Pixel layer; this procedure assumes that the bremsstrahlung occurs after the innermost measured point of the track.

The procedure is tested using electrons of 10 GeV/c and 40 GeV/c transverse momentum, generated in the pseudorapidity intervals $0.17 < \eta < 0.26$, close to the barrel centre, and $1.26 < \eta < 1.35$, near the end of the EM barrel, where a larger amount of material is encountered by particles traversing the Tracker. The p_T resolution we expect after the application of the recovery procedure is shown in Table 9.1; in the 4 T field, this measurement has an accuracy of about 5% at 10 GeV/c, limited by the angular resolution of the calorimeter. Better resolution should be achieved by the subsequent use of a Kalman filter that, starting from this momentum estimate, re-fits the whole track taking into account the emission of one bremsstrahlung photon.

[2]In the following, the notation E/p is used for E_T/p_T

9.4.1.2 Performance

Tracks are reconstructed using the GTF algorithm; the requirement that tracks have at least one hit in the Pixel detector will be referred to as a 'fiducial cut' in the following. The E/p distributions for the electrons in the four samples described in Table 9.1 are shown in Figs. 9.26 through 9.29; in each figure, the upper plot shows the raw distribution while the lower plot reports the corrected E/p distribution. The recovery of the non-Gaussian tail caused by bremsstrahlung is visible. The tails of the corrected E/p distributions are different in the $p_T = 10$ GeV/c and $p_T = 40$ GeV/c samples, reflecting the different momentum resolution for the two cases: at 10 GeV/c the recovered momentum and energy resolution are comparable with each other, whereas at 40 GeV/c the poorer resolution on the momentum yields symmetric tails in the E/p distributions.

The track reconstruction efficiencies before and after the fiducial requirement are shown in Table 9.2 and labelled as ϵ_{track} and $\epsilon_{track}^{fiducial}$ respectively. The fraction of fiducial tracks selected by the recovery procedure, $\mathcal{F}_{brems}$, is reported in the fourth column. The last two columns of Table 9.2 report the fraction of good quality tracks, i.e. those satisfying $0.85 < E/p < 1.2$, before and after recovering radiation losses ($\epsilon_{E/p}^{raw}$, $\epsilon_{E/p}^{corrected}$). The two fractions are evaluated with respect to the sample of fiducial tracks. At constant pseudorapidity, the fraction of radiated energy is independent of the electron momentum but, however, the reconstruction efficiency increases with p_T. This is due to the fact that the angle between the photon and electron directions at the emission point is smaller for higher p_T tracks, yielding a better hit collection efficiency. Conversely, the efficiency of the E/p cut is higher for the lower transverse momentum electrons, due to the better match between p_T and E_T resolution. At constant p_T, the fraction of re-fitted tracks is expected to increase with pseudorapidity, as bremsstrahlung effects become more significant. The values of ϵ_{track} reported in the table differ from the efficiency reported in Fig. 9.25 since this study of bremsstrahlung recovery was made using a less accurate description of the Tracker material budget.

Table 9.2: Track reconstruction efficiency before and after fiducial cut together with the fraction of re-fitted tracks and the efficiency of the E/p requirement.

p_T (GeV/c)	η	ϵ_{track} (%)	$\epsilon_{track}^{fiducial}$ (%)	$\mathcal{F}_{brems}$ (%)	$\epsilon_{E/p}^{raw}$ (%)	$\epsilon_{E/p}^{corrected}$ (%)
10	0.17-0.26	87.0	75	6.4	95.4	98.9
10	1.26-1.35	78.2	65	19.0	88.3	99.0
40	0.17-0.26	94.4	84.6	14.2	93.3	97.2
40	1.26-1.35	89.4	74.8	39.8	83.4	90.1

The efficiencies for reconstructing fiducial tracks with GTF are only $\sim 70\%$ in the 10 GeV/c sample and $\sim 80\%$ in the 40 GeV/c sample. The global efficiency of the recovery procedure is penalised by the fact that electrons undergoing large energy losses are often reconstructed only in the outermost part of the Tracker and fail the fiducial selection. To improve the electron reconstruction performance, the electron samples have been re-analysed relaxing the GTF cuts. This results in a non negligible fraction of events with more than one reconstructed track per generated electron (in the previous analysis this fraction vanished) in which case the track with the highest p_T is chosen. The E/p distributions before and after the recovery procedure are shown in Figs. 9.30 through 9.33. The tails of the raw distributions are much larger than in the previous study, as was to be expected.

The efficiencies of track reconstruction, fiducial selection and E/p cut are shown in Table 9.3. The electron reconstruction efficiency is substantially improved and typically more than 90% of

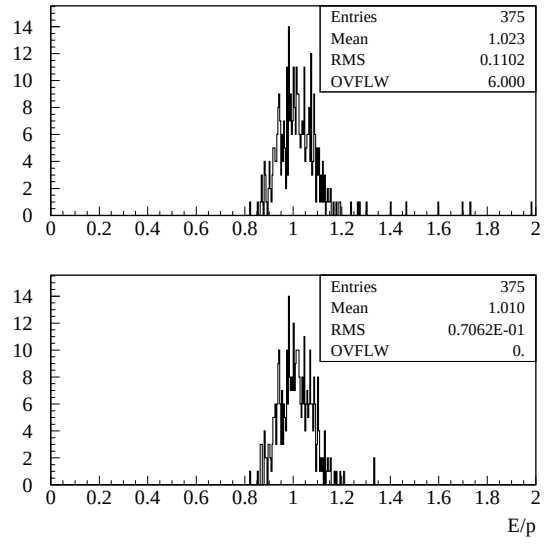

Fig. 9.26: E/p distribution before (top) and after (bottom) radiation recovery, for 10 GeV/c p_T electrons in $0.17 < \eta < 0.26$, reconstructed with GTF cuts.

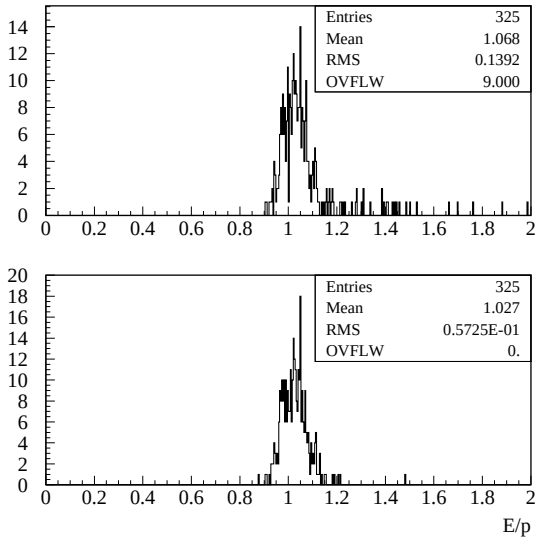

Fig. 9.27: E/p distribution before (top) and after (bottom) radiation recovery, for 10 GeV/c p_T electrons in $1.26 < \eta < 1.35$, reconstructed with GTF cuts.

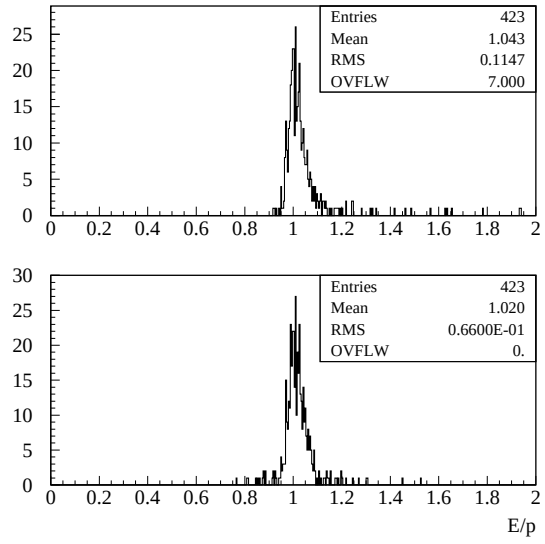

Fig. 9.28: Same as Fig. 9.26, for 40 GeV/c p_T electrons.

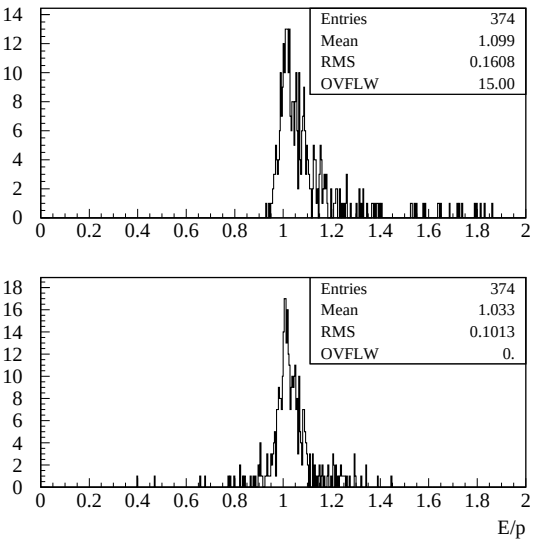

Fig. 9.29: Same as Fig. 9.27, for 40 GeV/c p_T electrons.

the tracks are now fiducial. The efficiency of bremsstrahlung recovery, defined as $\epsilon_{E/p}^{corrected} - \epsilon_{E/p}^{raw}$, has increased by a factor close to three: from 6% to 17% at small η and from 15% to 35% at large η. After correction of the track curvature, more than 95% of the electrons have values of E/p in the selected range. We report in Table 9.4 a study of the sensitivity of the recovery procedure to the assumptions made on the EM calorimeter performance.

This feasibility study shows that the transverse momentum of more than 90% of the generated electrons can be measured without the bias induced by the energy losses in the Tracker material. For more than 95% of the reconstructed electrons the E/p ratio is in the range $0.85 \leq E/p \leq 1.2$. The E/p resolution is dominated by the corrected p_T resolution for electron energies larger

than 10 GeV/c. More sophisticated reconstruction strategies, that improve the accuracy of the transverse momentum estimate, will be the object of future work.

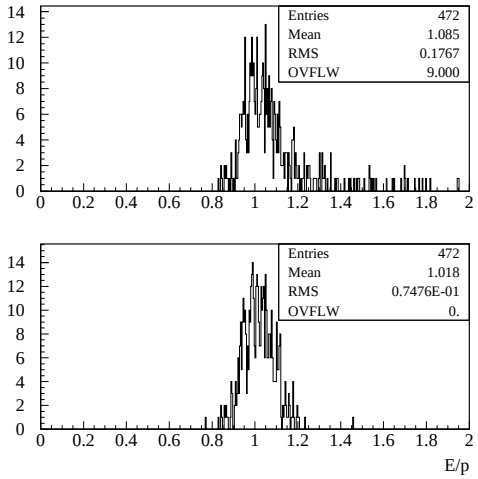

Fig. 9.30: E/p distribution before (top) and after (bottom) recovery, for 10 GeV/c p_T electrons in $0.17 < \eta < 0.26$ and using loose GTF.

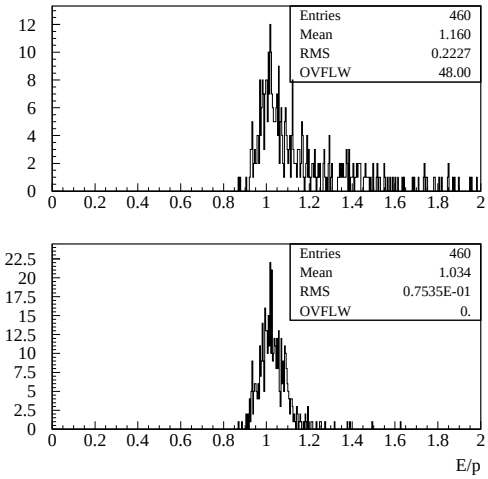

Fig. 9.31: E/p distribution before (top) and after (bottom) radiation recovery, for 10 GeV/c p_T electrons in $1.26 < \eta < 1.35$ and using loose GTF.

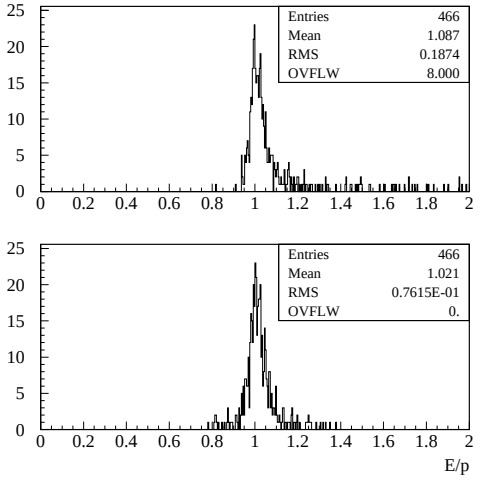

Fig. 9.32: Same as Fig. 9.30, for 40 GeV/c p_T electrons.

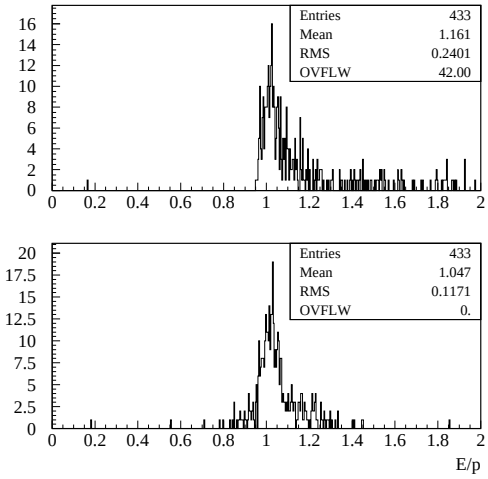

Fig. 9.33: Same as Fig. 9.31, for 40 GeV/c p_T electrons.

Table 9.3: Track reconstruction efficiency before and after fiducial cut, fraction of re-fitted tracks and efficiency of the E/p cut ($0.85 \leq \eta \leq 1.2$). Tracks are reconstructed with GTF, using looser reconstruction cuts than in previous tables, as discussed in the text

p_T (GeV/c)	η	ϵ_{track} (%)	$\epsilon_{track}^{fiducial}$ (%)	$\mathcal{F}_{brems}$ (%)	$\epsilon_{E/p}^{raw}$ (%)	$\epsilon_{E/p}^{corrected}$ (%)
10	0.17-0.26	97.3	94.4	25.6	82.8	98.0
10	1.26-1.35	96.2	92.0	50.0	64.1	97.6
40	0.17-0.26	99.2	93.2	25.1	85.6	94.8
40	1.26-1.35	97.4	86.6	51.0	67.4	88.6

Table 9.4: Efficiency of the E/p cut before and after bremsstrahlung recovery, for 10 GeV/c and 40 GeV/c p_T electrons at $\eta = 1.26$-1.35, for different assumptions on the energy and position resolution.

p_T (GeV/c)	η	σ_E (GeV/c)	σ_ϕ (mrad)	$\epsilon_{E/p}^{raw}$ (%)	$\epsilon_{E/p}^{corrected}$ (%)
10	1.26-1.35	0.26	1.13	62.3	98.4
		0.78	3.39	64.1	97.6
		0.78	6.78	63.2	95.6
40	1.26-1.35	0.53	0.99	67.6	95.3
		1.59	2.96	67.4	88.6
		1.59	5.90	67.8	76.0

9.4.2 Hadron reconstruction

9.4.2.1 Definition of efficiency

As discussed in Chapter 7 (Fig. 7.31), hadron interactions with the Tracker material must be taken into account: the average fraction of pions interacting inelastically in the interval $|\eta| \leq 2.4$ varies between 17.5% at 1 GeV/c p_T and 14% at 5 GeV/c p_T. Early interactions generate very short tracks in the detector, which are reconstructed with low efficiency by GTF and CM. To simplify the discussion, we recall here the definition of tracking efficiency:

$$\epsilon_{H,P} = \frac{N \text{ reconstructed associated tracks}}{N \text{ generated primary tracks}}$$

where tracks may be associated to the parent helix by 1) the requirement that they share at least 50% of the hits (ϵ_H), or by 2) the requirement that all track parameters differ from their true value by less than five times their fitted error (ϵ_P). An implicit requirement that there be at least six hits per reconstructed track is applied. To unfold the contribution of early interactions from the definition of efficiency, a different estimator is used: $\epsilon_{H,P}^{g6}$ is defined by comparing the reconstructed and associated tracks to the subset of the generated helices that have at least six impacts in the Tracker; an impact is defined here as the intersection between a helix and a sensor in the detector. For GTF, the six impacts have to satisfy the topological requirements discussed in Section 8.1.1, e.g. at least one impact should be in the Outer Layers and one in the Middle Layers to seed the track reconstruction procedure. In the following, $\epsilon_{H,P}^{g6}$ will be estimated with respect to those helices with at least six hits that fulfil the GTF pattern requirement.

9.4.2.2 Performance

A study of the track finding efficiency for pions of several transverse momenta was carried out using GTF and the Phase II detector; in Figs. 9.34a and 9.34b the efficiencies for reconstructing single pions, ϵ_H^{g6} and ϵ_H, are shown as a function of pseudorapidity. In Figs. 9.34c and 9.34d ϵ_P^{g6} and ϵ_P are similarly shown. The track finder is fully efficient for hard pions which collect at

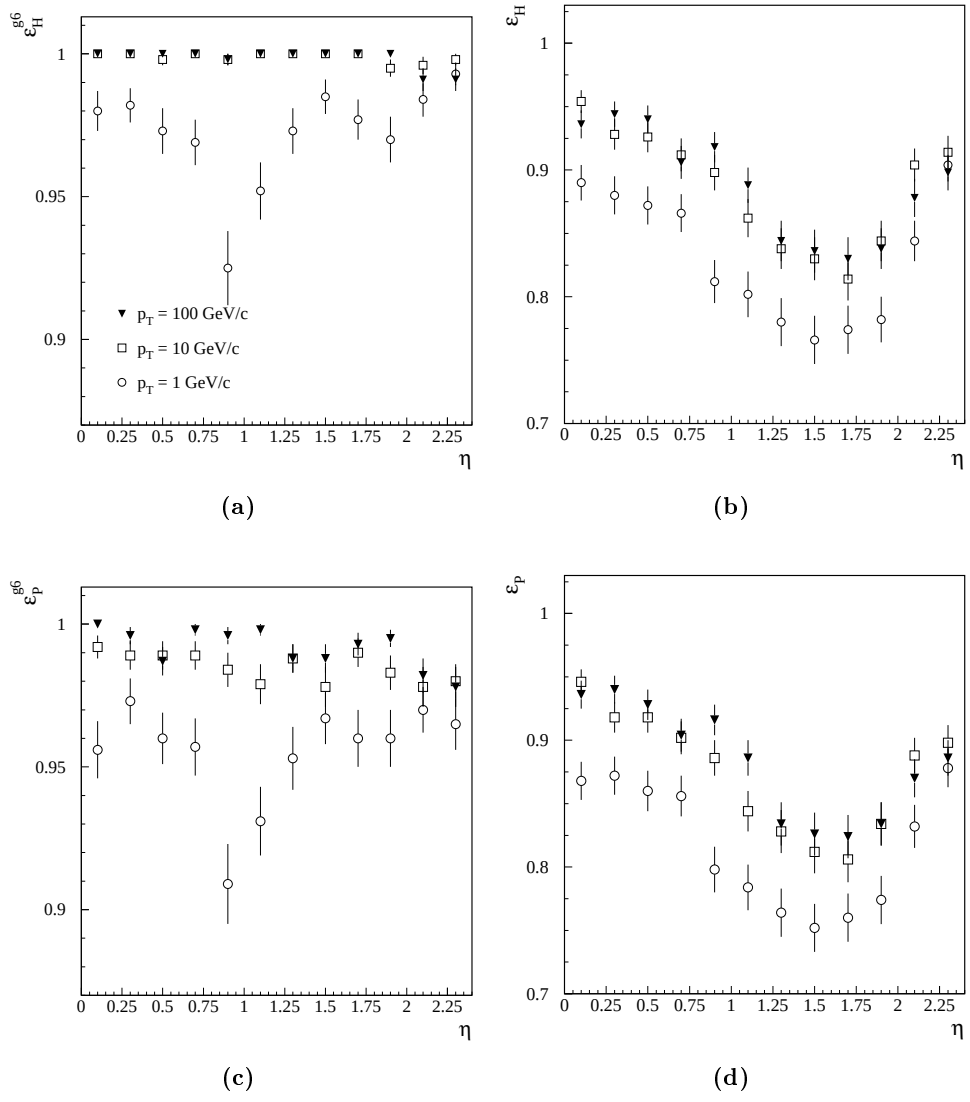

Fig. 9.34: Track finding efficiency for single pions as a function of pseudorapidity, for three different values of the transverse momentum. In (a) and (b) the association between generated and reconstructed track is based on the number of shared hits, in (c) and (d) on the accuracy of the track fit. The intrinsic performance of the track finder is shown in (a) and (c) while (b) and (d) show the global probability of reconstructing a generated track. Phase II detector layout.

least six hits in the Tracker (plot a). An efficiency drop of $2 \div 3\%$ is observed for pions of $p_T = 1$ GeV/c, increasing to $7 \div 8\%$ in the vicinity of the gap between the MSGC barrel and endcaps. The fraction of tracks that interact before depositing the required six hit pattern in the detector amounts to $5 \div 15\%$, depending on η (plots b and d). The η dependence of the inefficiency is obviously correlated to the amount of material that the particles traverse at different angles.

The quality of the hadron fit is worse than for muons, resulting in a loss of efficiency of $1 \div 2\%$ when the association is based on the accuracy of the fitted track parameters (plot c).

The pion study has been repeated for the Phase I Tracker and its results are shown in Fig. 9.35. The overall behaviour is very similar for the two Tracker layouts. The efficiency ϵ_H estimated with GTF in the Phase I detector is compatible within errors with the efficiency estimated using the Phase II layout, because the reduced tracking capability is compensated by a small reduction of the material budget. A preliminary study that relies on the Forward Kalman

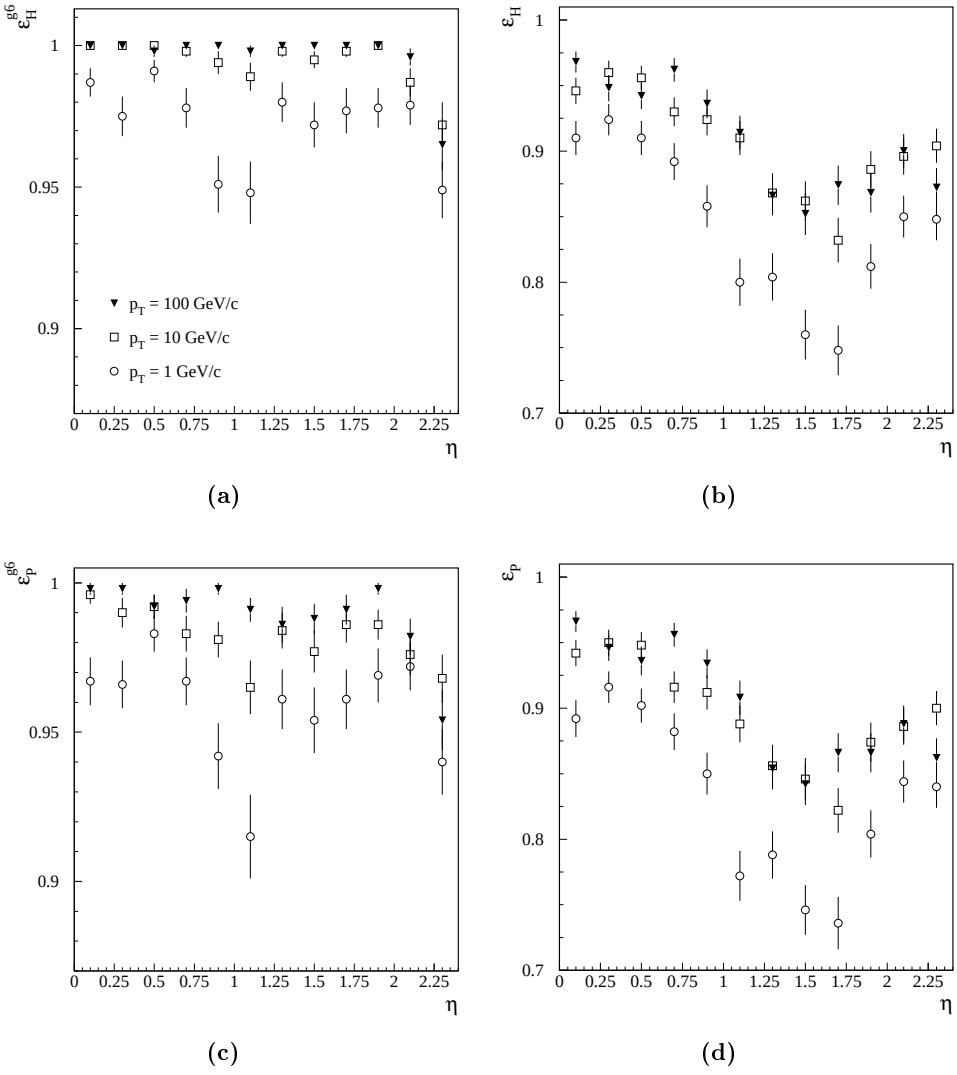

Fig. 9.35: Same study as in Fig. 9.34 for the Phase I detector configuration.

Filter algorithm (FKF) and CM[3] shows that a substantial fraction of the pion reconstruction inefficiency observed using GTF can be recovered. For FKF, the restrictions on the topology of the six impacts required for a track to be 'reconstructible', are largely relaxed. Consequently, the fraction of track candidates examined by FKF is increased with respect to GTF.

We show in Fig. 9.36 ϵ_H for muons and pions, obtained with the FKF algorithm and the Phase I configuration of the Tracker. The efficiency for muons is only slightly better than the

[3]To reconstruct hadron tracks we use FKF in the forward propagation phase and CM for the backward propagation procedure.

one obtained using GTF, while in the case of pions a substantial improvement can be observed (compare with Fig. 9.35b), due to the ability of this algorithm to reconstruct hadrons which interact in the outer silicon layers. The improvement is particularly large in the region $1 < \eta < 2$, where the performance of GTF is limited by the amount of material in the Tracker. In this region the gain in efficiency is of the order of $8 \div 10\%$, which corresponds to a reduction of the inefficiency by more than a factor of two. At the largest $|\eta|$ the track finding performance is affected by the smaller number of detectors, and the gain is more moderate. The recovery of reconstruction efficiency is expected to be even larger in the case of the Phase II Tracker, which provides more measuring stations and has a slightly larger material budget.

The average global efficiency for hadron reconstruction is larger than 90 %. This shows that a sizeable improvement in this efficiency can be achieved by using dedicated techniques.

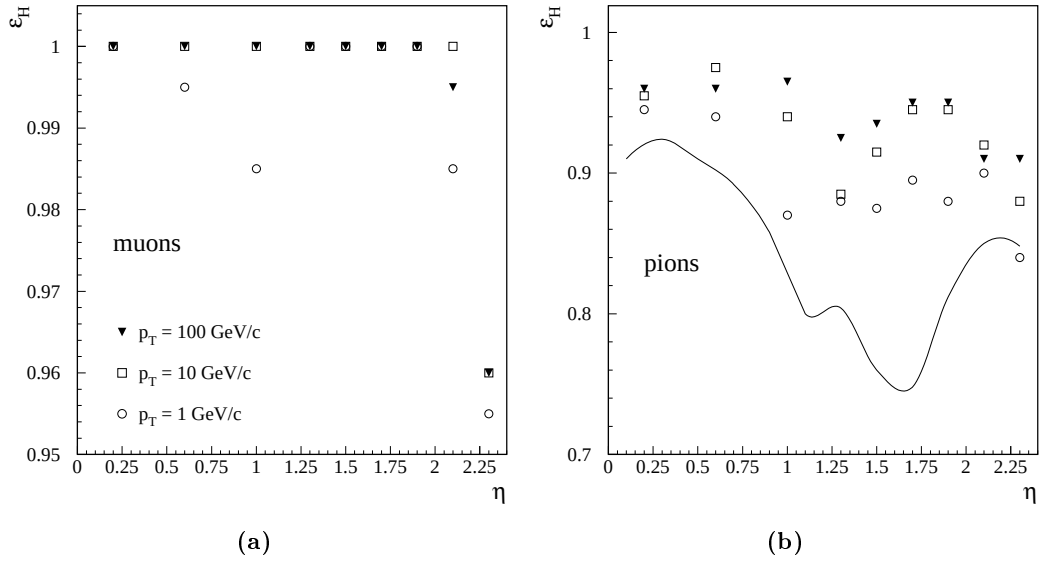

Fig. 9.36: Track finding efficiency for (a) muons (b) pions reconstructed with the Forward Kalman Filter algorithm in the Phase I detector. The solid line in (b) shows the performance of GTF. The efficiency is defined on the basis of the hits shared by the track and the parent helix.

9.4.2.3 Tails of distributions

Good reconstruction of low transverse momentum pions plays an important role in B-physics, e.g. for the reconstruction of B meson decays, and in the identification of b-jets. We test the quality of the track reconstruction by studying the tails of the transverse impact parameter and curvature pull distributions for 1 GeV/c p_T pions, as in Section 9.3.6. The tail fractions are shown in Fig. 9.37 as a function of pseudorapidity; the tail fractions for muons are also shown for ease of comparison. Muons and pions are required to register at least two hits in the Pixel detector. A non-Gaussian tail of less than 1% is observed for the pull of the $1/p_T$ variable, independent of η. The tail fraction of x_{imp} does not exceed 2%. Muon and pion tracks are reconstructed with equal accuracy.

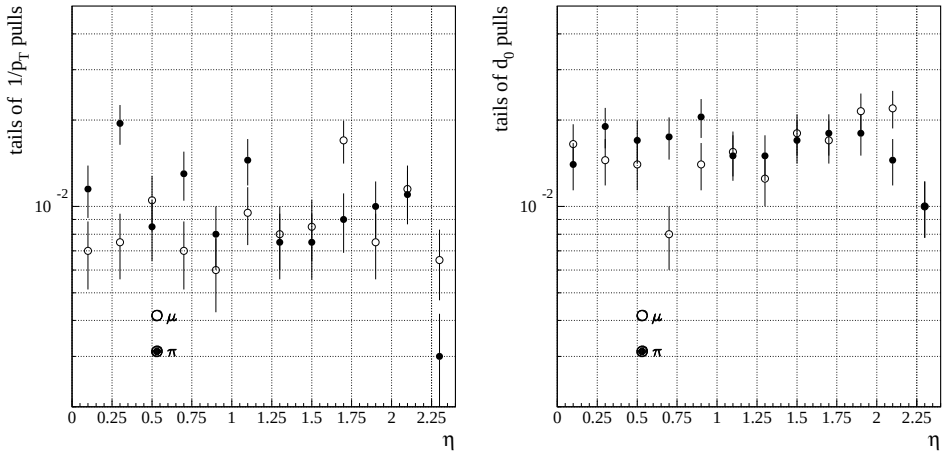

(a) (b)

Fig. 9.37: Tail fraction of the $1/p_T$ and x_{imp} pull distributions for 1 GeV/c p_T pions and muons as a function of pseudorapidity. Tracks are reconstructed using GTF; all tracks are required to have at least two hits in the Pixel detectors.

9.5 Tracks in Jets

9.5.1 Occupancy inside high p_T jets

To probe the environment in which our track finding algorithms must work, it is useful to study the occupancy within high p_T jets, representative of the topology of several physics reactions that will be studied at the LHC. Hard $b\bar{b}$ events were generated embedding 200 GeV transverse energy jets into the minimum bias pile-up events defined in Section 7.11, for high luminosity running conditions. The local occupancy (Section 7.11.2.1) reported in Fig. 9.38 is evaluated by using all clusters in detector centred within the window

$$|\Delta\phi| \leq 0.1, \quad |\Delta\eta| \leq 0.1$$

around the jet axis, defined by the direction of flight of the b quark. The local occupancy contributed by the pile-up alone is shown separately by a solid line. The local occupancies observed inside jets in the Silicon barrel detector are up to $\sim 30\%$ higher than those observed in minimum bias pile-up events. A lesser increase ($\sim 15\%$) is observed in the local MSGC occupancy. The r.m.s. width of each of these distributions is approximately 80% of its mean value.

9.5.1.1 Cluster quality

In a dense environment a wrong cluster may be attached to the track candidate, or it may happen that clusters are produced by overlapping particles. These phenomena will cause either loss of efficiency or mis-measurement of the track helix. There are three relevant factors in this context: the intrinsic hit quality, the 'road size' of the pattern recognition, and the occupancy contributed by spurious hits within the road.

Hit quality is characterised for each cluster by comparing its distance from the parent impact with the intrinsic hit resolution (σ_{res}) of the detector. If the residual distribution has sizeable tails, extending beyond the search road, the hits may be missed, or replaced by wrong ones.

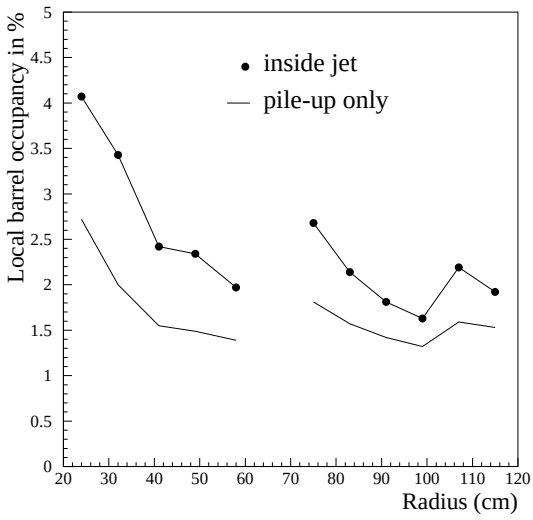

Fig. 9.38: Local barrel occupancy within 200 GeV E_T jets, in high luminosity LHC events recorded by the CMS Tracker. The pile-up contribution is shown separately (solid line).

Once the track is correctly seeded, the comparison between σ_{res}, the tail fractions and the size of the pattern recognition road illustrates the ability of the reconstruction and fitting procedure to choose good hits.

Table 9.5 summarises the σ_{res} and road sizes for the barrel detectors. To measure σ_{res}, reported in the second column, stiff tracks have been embedded inside the high p_T jets in the sample previously described. The intrinsic resolution is extracted by fitting the core of the hit residual distribution with a Gaussian function. The third and fourth columns show the fraction of hits reconstructed at a distance larger than three and five σ_{res} from the parent impact, respectively. In the fourth and fifth columns, the size of the roads used in the preliminary search of the pattern recognition and in the final iteration of the track fit are shown. The size of the road used for the initial search reflects the Kalman filter track finding strategy used by CM and GTF. Kalman filtering becomes selective only after the first few steps. At the earliest stages

Table 9.5: Resolution, tail fraction and track reconstruction roads in the CMS Tracker

Barrel layer	σ_{res} (μm)	Tail fraction $3\sigma_{res}$ (%)	Tail fraction $5\sigma_{res}$ (%)	Initial search road size (μm)	Fit road road size (μm)
Silicon - 1	13.5	8.9	5.5	272	67.0
Silicon - 2	18.8	6.2	3.8	301	83.0
Silicon - 3	18.7	4.6	3.0	509	96.0
Silicon - 4	27.9	3.9	2.4	490	111.0
Silicon - 5	28.5	3.7	2.2	1180	124.0
MSGC - 1	30.4	7.1	3.7	830	116.0
MSGC - 2	29.3	6.1	3.2	1230	119.0
MSGC - 3	29.8	6.9	3.2	2000	125.0
MSGC - 4	29.5	6.3	3.4	2000	150.0
MSGC - 5	29.5	5.7	2.9	2000	205.0
MSGC - 6	29.7	5.5	2.5		286.0

the combinatorial background can be large and fake track seeds can easily be generated in the high hit density environment found within jets. Once a track is correctly initialised, the pattern recognition road is fully efficient. The road used in the final fit (smoothing) is based on realistic error estimates and has rejection power. Clusters within $3\,\sigma_{res}$ and $5\,\sigma_{res}$ of their true position,

typically 3%, can deform the fitted helix and are partially rejected by the fitting procedure whereas most distant hits (3-6%) are mostly dropped. The non-Gaussian tails of the residual distribution are due to cluster splitting, cluster merging and to badly reconstructed hits. The 5-σ_{res} tail fraction is greatest at the innermost radius of the Tracker, where it is most affected by the presence of high luminosity pile-up.

9.5.2 Track finding performance

The efficiency to reconstruct tracks within high p_T jets is investigated using the event samples described in Section 9.2.4. The definition of efficiency used in this study is

$$\epsilon_H = \frac{\text{N reconstructed associated tracks}}{\text{N fiducial generated tracks}}$$

The reconstructed tracks are associated to the parent helix if they share more than 50% of the hits. Generated and reconstructed tracks are selected by several fiducial requirements, reported in Table 9.6. The symbols V_T and V_z represent the position of the generated event vertex in the transverse plane and along the z-axis, respectively. Looser fiducial cuts are imposed on the reconstructed tracks to allow for the finite accuracy of the track parameter measurement. The track fake rate ϵ_{fake} is defined as the fraction of non-associated reconstructed tracks. In this case the fiducial requirements for the generated and reconstructed tracks are reversed.

Table 9.6: Preselection requirements used to define the track finding efficiency.

Generated tracks	Reconstructed tracks
$p_T \geq 0.9$	$p_T \geq 0.7$
$\|\eta\| \leq 2.5$	$\|\eta\| \leq 2.6$
$V_T \leq 3$ cm	no cut on $\|d_0\|$
$\|V_z\| \leq 30$ cm	no cut $\|z_{imp}\|$

The performance of the CMS Tracker is studied using the GTF and CM track finding algorithms. The GTF reconstruction procedure requires tracks to have at least eight hits. The CM and FKF track finders are combined and used for backward and forward propagation, respectively. We shall refer to this combination simply as CM-FKF. The minimum number of hits required by CM-FKF is six and a χ^2 cut is imposed, $\chi^2/\text{ndf} \leq 7$. No smoothing procedure is applied. The reconstruction efficiency for tracks within $R = \sqrt{\Delta\eta^2 + \Delta\phi^2} = 0.4$ from the jet axis is shown in Figs. 9.39 and 9.40 as a function of the jet pseudorapidity. In the barrel part of the Tracker we estimate an efficiency ϵ_H larger than 93%. The efficiency decreases by 8-10% at larger pseudorapidity values. The behaviour of ϵ_H as a function of η is accounted for by the decrease of the hadron reconstruction efficiency at $|\eta| \geq 0.7$. This study must be compared to the one reported in Fig. 9.36b, which also explains the different ability of CM-FKF and GTF to reconstruct tracks within jets. Within the errors, ϵ_H is fairly independent of the jet E_T. The average efficiency estimated using 200 GeV E_T jets tends nevertheless to be 2-3% lower than the ones measured using softer jets. The track fake rate estimated for the Phase I Tracker is shown in Figs. 9.41 and 9.42 for CM-FKF and GTF. We estimate a track fake rate lower than 0.5% in all the event samples, when using GTF. The track fake rate depends only weakly on η. We measure instead a significant dependence of ϵ_{fake} on the jet E_T, obviously correlated to the larger track multiplicity and density within jets of increasing transverse energy. The values of ϵ_{fake} estimated using CM-FKF are larger than for GTF. In fact, the track selection used by GTF biases the track candidate samples to contain higher quality tracks than those preselected by CM-FKF, which pays a small price for a much higher track finding efficiency than GTF. We performed a similar study using GTF and the Phase II Tracker layout. The values of ϵ_H and

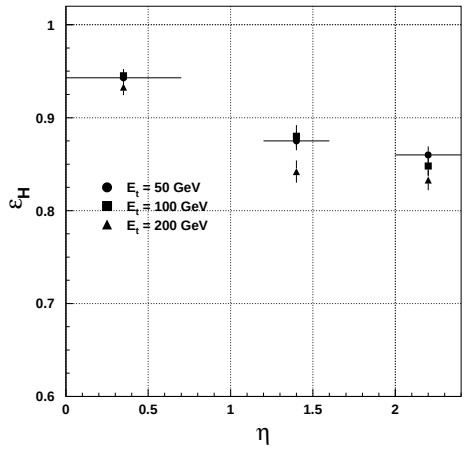

Fig. 9.39: Track reconstruction efficiency within jets as a function of jet pseudorapidity. Tracks are reconstructed with CM-FKF in the Phase I Tracker.

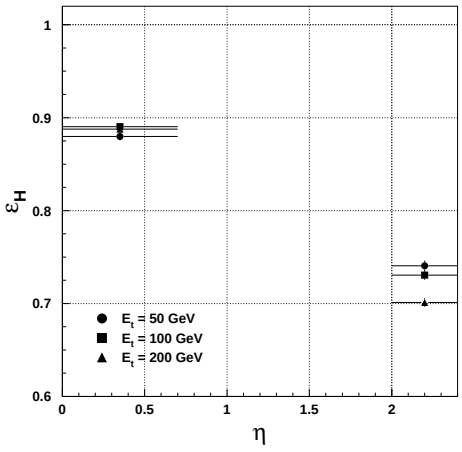

Fig. 9.40: Track reconstruction efficiency within jets as a function of jet pseudorapidity. Tracks are reconstructed with GTF in the Phase I Tracker.

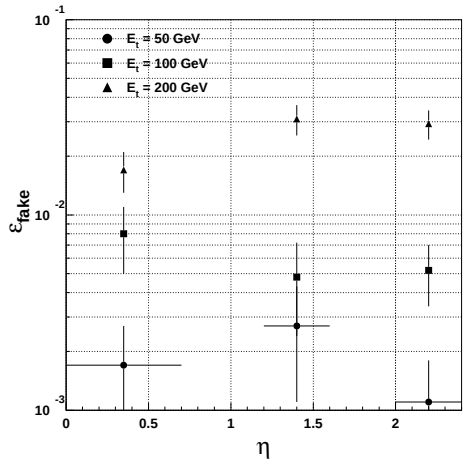

Fig. 9.41: Track fake rate within jets as a function of jet pseudorapidity and transverse energy. Tracks are reconstructed with CM-FKF in the Phase I Tracker.

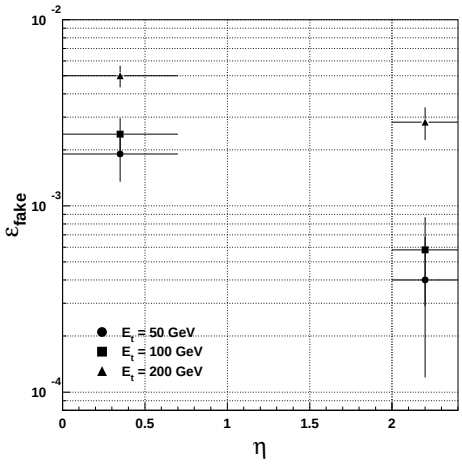

Fig. 9.42: Track fake rate within jets as a function of jet pseudorapidity and transverse energy. Tracks are reconstructed with GTF in the Phase I Tracker.

ϵ_{fake} are shown in Figs. 9.43 and 9.44. The track finding efficiencies are higher than the values measured using the Phase I detector. The ϵ_H estimate at large η is improved by $\sim 10\%$, due to the increased number of measuring stations available in the Phase II Tracker. The values of ϵ_{fake} are reduced by a factor of 1.5-2.0.

The efficiency to reconstruct tracks within jets at high luminosity conditions is shown in Fig. 9.45. The ϵ_H values are the same that we measured in absence of pile-up. The fake rate is in this case about 1% and a detailed study is presently under way.

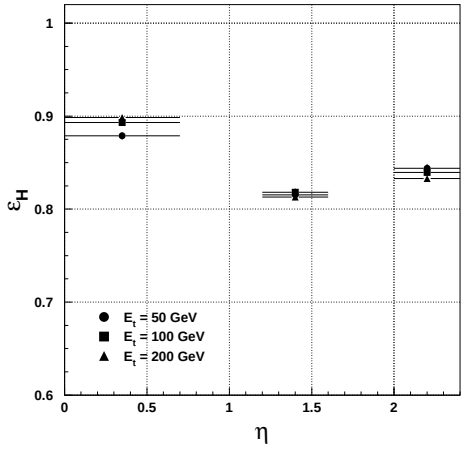

Fig. 9.43: Track finding efficiency within jets as a function of jet pseudorapidity and transverse energy. Tracks are reconstructed with GTF in the Phase II Tracker.

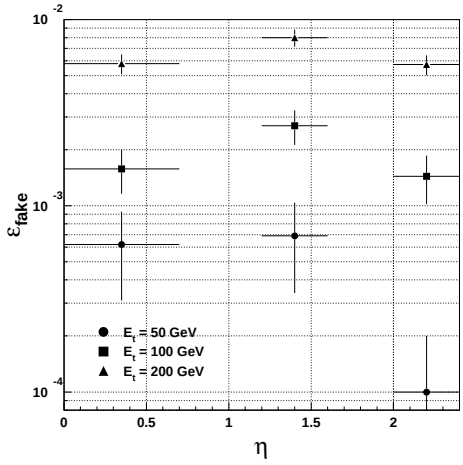

Fig. 9.44: Track fake rate within jets as a function of jet pseudorapidity and transverse energy. Tracks are reconstructed with GTF in the Phase II Tracker.

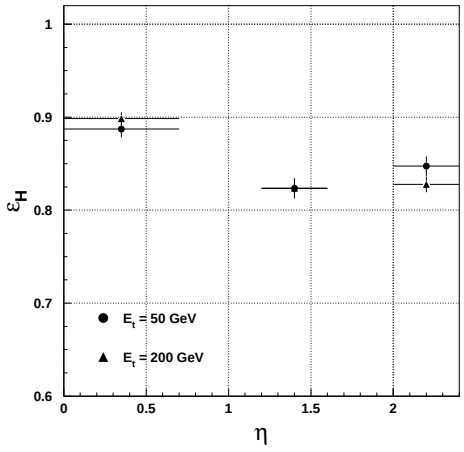

Fig. 9.45: Track finding efficiency within jets in high luminosity events, as a function of jet pseudorapidity and transverse energy. Tracks are reconstructed with GTF in the Phase II Tracker.

9.6 Vertex Reconstruction

9.6.1 Primary vertices

Our studies indicate that primary vertex location is indeed simple provided there are enough high p_T tracks in the event. To illustrate the primary vertex resolution measured with the CMS Tracker, a sample of 50 GeV E_T $u\bar{u}$ jets was generated at $|\eta| \leq 0.7$. Tracks are reconstructed using the FKF algorithm. The GVF algorithm was forced to reconstruct just primary vertices and only the tracks with impact parameter errors less than 100 μm were selected for the vertex search. The collision point is generated using Gaussian distributions of transverse spread of $\sigma_x = \sigma_y = 15$ μm and longitudinal spread of $\sigma_z = 5.3$ cm. The primary vertex resolution is shown in Figs. 9.46 through 9.49 for the Phase I and II Trackers, respectively. For this particular event

sample the z coordinate resolution is about 32 μm (26 μm) for the Phase II (Phase I) Tracker. The resolution in the transverse plane is quite comparable with the transverse beam position smearing.

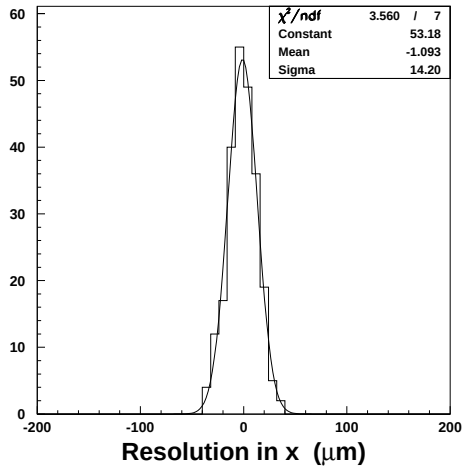

Fig. 9.46: Resolution of the x-coordinate of the primary vertex in di-jet events. Phase I Tracker.

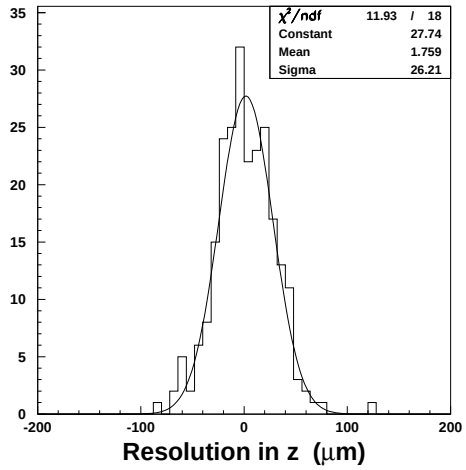

Fig. 9.47: Resolution of the z-coordinate of the primary vertex in di-jet events. Phase I Tracker.

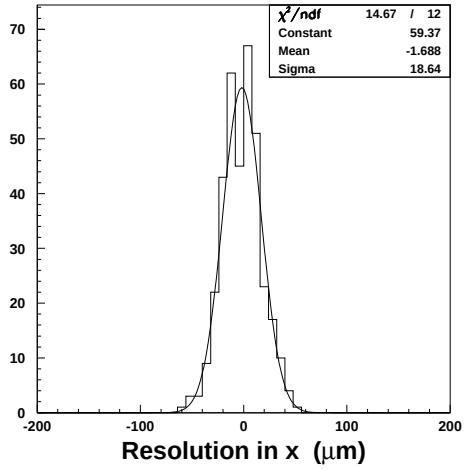

Fig. 9.48: Resolution of the x-coordinate of the primary vertex in di-jet events. Phase II Tracker.

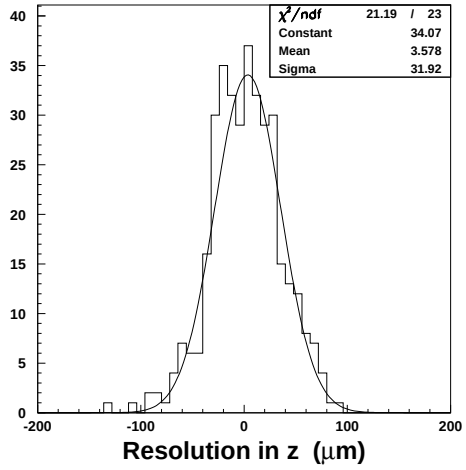

Fig. 9.49: Resolution of the z-coordinate of the primary vertex in di-jet events. Phase II Tracker.

The primary vertex resolution for $H \to \gamma\gamma$ events is studied by the PVF and GVF algorithms. The Higgs events are produced by the $gg \to H$ and the vector boson fusion production mechanisms, using the PYTHIA event generator and $m_H = 100$ GeV/c^2. The result are shown in Figs. 9.50 and 9.51, where the difference between the simulated and fitted vertex position

in z is plotted for the Phase I Tracker. Only charged tracks with $p_T > 0.6$ GeV/c are used for fitting by PVF, whereas GVF reconstructs tracks with FKF and no explicit cut on the track transverse momenta. The central part of the distributions is fitted with a Gaussian function, yielding a resolution of about 50 μm for PVF and about 60 μm for GVF. The non-Gaussian tails in the PVF distribution represent the cases for which the number of large p_T tracks is small. The efficiency of the $H \to \gamma\gamma$ event vertex finding is 100%.

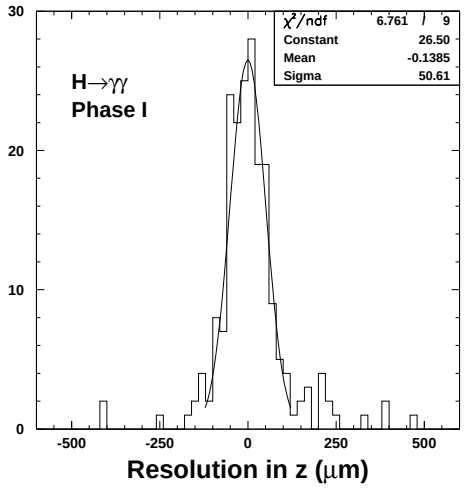

Fig. 9.50: Resolution of the z-coordinate of the primary vertex in $H \to \gamma\gamma$ events reconstructed by PVF in the Phase I Tracker.

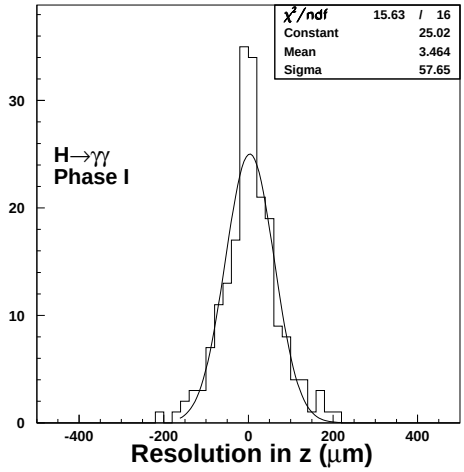

Fig. 9.51: Resolution of the z-coordinate of the primary vertex in $H \to \gamma\gamma$ events reconstructed by GVF in the Phase I Tracker.

9.6.2 V^0 vertices

9.6.2.1 Reconstruction of converted photons

As mentioned in Chapter 7, a large fraction of photons undergo conversion before leaving the sensitive volume of the Tracker. Some of the converted photons can be recovered by reconstructing the e^+e^- pair. A study of the reconstruction efficiency is performed using a sample of 10^5 photons of $p_T = 30$ GeV/c generated at $|\eta| < 0.7$. The fraction of converted photons in the central Tracker volume is found to be 20% and 22%, for the Phase I and Phase II detectors, respectively.

Tracks are reconstructed using GTF for the Phase I layout and both GTF and CM algorithms for the Phase II Tracker. The two track finders require at least six clusters along the reconstructed track. After two tracks of opposite sign have been selected, CM requires a secondary vertex to be reconstructed by GVF. The GTF efficiency to reconstruct converted photons is 29% in the Phase I detector, affected by a reduced number of measuring stations at the outer radii of the barrel. We report the efficiencies of the two methods for the Phase II Tracker in Table 9.7. The first row in the table represents the efficiency of the requirements imposed by GTF and CM for an e^+e^- pair to be 'reconstructible'. About 30% of the conversions occur at large radii and cannot be reconstructed. The second row shows the efficiency of the algorithms, i.e. the efficiency to reconstruct a preselected converted photon. The intrinsic efficiency of the track finders is obviously affected by bremsstrahlung effects, and part of the inefficiency can be suppressed by applying bremsstrahlung recovery corrections. The performance of CM is superior

Table 9.7: Efficiency of track selection criteria, intrinsic track finder efficiency and global efficiency to reconstruct photons undergoing conversion in the Phase II Tracker detector

Reconstruction algorithm	GTF	CM+GVF
Fraction of preselected photons (%)	70	
Algorithm reconstruction efficiency (%)	50	70
Global reconstruction efficiency (%)	35	50

to the one of GTF, which is biased by an initial pattern recognition road defined using the beam constraint. We report in the third row the global reconstruction efficiency, which amounts to 50% for the photons that convert in the barrel.

Once the e^+e^- pair is reconstructed, the coordinates of the photon emission point can be estimated (z^{γ}_{imp}). The obtained z^{γ}_{imp} resolution is shown in Fig. 9.52. Three different populations contribute to the z_{imp} distribution. The central part is due to very early conversions for which the Pixel detector can measure z^{γ}_{imp} with an accuracy of 75 μm in $\sim 15\%$ of the cases. The other components are contributed by conversions occurring in detectors at larger radii or in the passive volumes inside the Tracker. The r.m.s. of the overall distribution is ~ 2.6 mm. Photons whose origin is reconstructed with a precision better than 1 centimetre can be used to determine the position of the primary vertex of the reaction $H \to \gamma\gamma$. The accuracy of the z^{γ}_{imp} measurement is satisfactory for all the reconstructed photons that convert in the barrel of the Phase II Tracker.

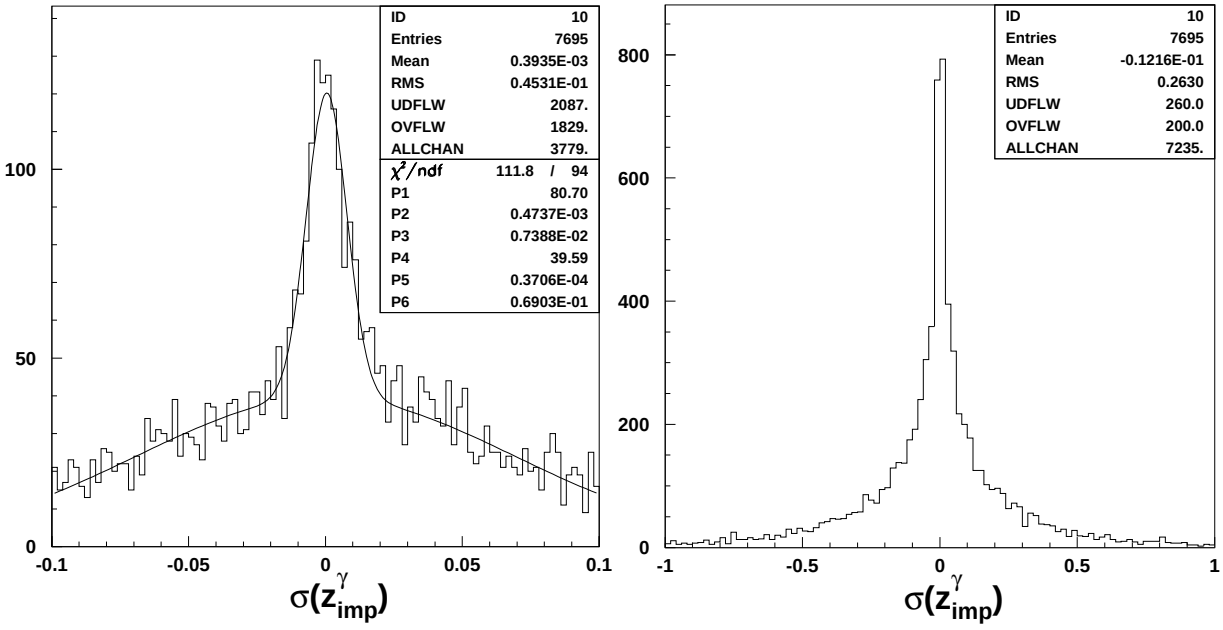

Fig. 9.52: Resolution on the z impact point of the converted photon in the Phase II Tracker layout.

9.6.2.2 K^0_S reconstruction

The V^0 reconstruction performance is tested here using samples of K^0_S generated uniformly in η with p_T values ranging between 2 GeV/c and 15 GeV/c. The Phase I Tracker is used in this study. The CM algorithm is used to reconstruct the pion tracks from K^0_S decay. The tracks are required to have at least six hits and $\chi^2/\mathrm{ndf} < 7$. Once two tracks are reconstructed, the GVF algorithm is used to reconstruct K^0_S vertex. The K^0_S candidates are accepted if the reconstructed

mass is within 25 MeV/c^2 of the K^0_S mass and the reconstructed vertex is at least $3\sigma_D$ away from (0,0) in the transverse plane, σ_D being the error on the transverse decay distance. Alternatively, when $3\sigma_D \leq 1$ cm, an explicit cut of 1 cm is used.

The reconstruction efficiency is defined as the ratio of the number of reconstructed K^0_S to the total number of generated events. No cuts on the pion p_T and K^0_S decay position are applied at the generation level, i.e. global reconstruction efficiency is estimated.

The K^0_S reconstruction efficiency as a function of pseudorapidity is shown in Fig. 9.53 For the K^0_S's generated by primary B-mesons, the efficiency is typically 50% when the decays occur in the barrel Tracker and 33% in the remaining cases. The loss of reconstruction efficiency in the region $|\eta| \geq 0.8$ results mainly from the reduced number of measuring stations in the endcaps of the Phase I detector. Additional inefficiency is due to the low efficiency of the CM track finder for tracks of $p_T \leq 0.9$ GeV/c, which characterise the low p_T kaon decays.

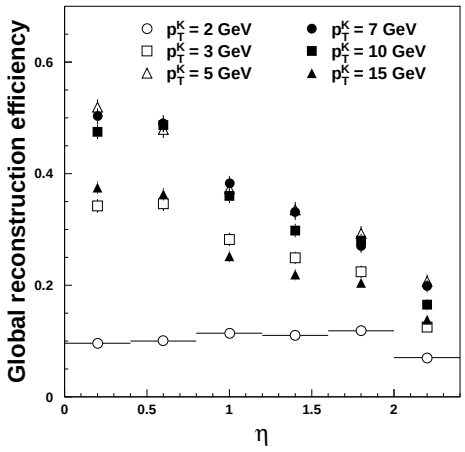

Fig. 9.53: K^0_S reconstruction efficiency as a function of η in the Phase I Tracker detector.

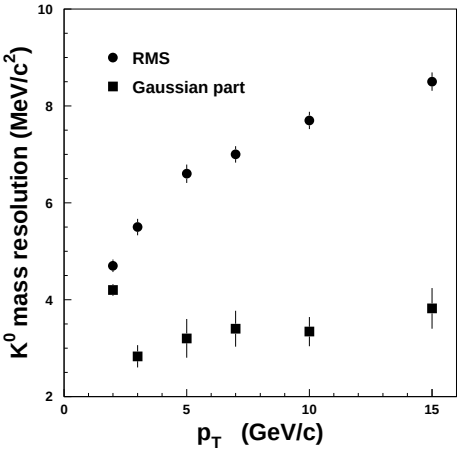

Fig. 9.54: K^0_S reconstructed mass resolution as a function of the K^0_S transverse momentum.

The reconstructed mass resolution, obtained by fitting the Gaussian part of the distribution, is about 3 MeV/c^2 and it is fairly independent of the K^0_S transverse momentum. The r.m.s. of the mass distribution varies by a factor of two as the transverse momentum of the K^0_S increases from 2 GeV/c to 15 GeV/c; the fraction of events in the 3σ-tails of the mass distribution is about 20% for K^0_S's with p_T in the range 3-7 GeV/c, and 25% for larger p_T. The characteristic p_T of K^0_S's from B-meson decay is approximately 5 GeV/c. The accuracy of the decay vertex reconstruction depends on the position at which the decay occurred: as shown in Fig. 9.56, the position resolution is ~ 0.27 mm for the early decays measured by precise detectors and about 2 mm in the remaining cases.

9.6.3 Reconstruction of $B \to J/\psi K_S$

The $B^0_d \to J/\psi K^0_S \to \mu\mu\pi\pi$ decay is a clean channel to measure $\sin 2\beta$ for CP violation studies. The event samples described in Section 9.2.3 are used to illustrate the performance of the Phase I Tracker. The following steps have been followed to reconstruct the sample of $B^0_d \to J/\psi K^0_S$ decays:

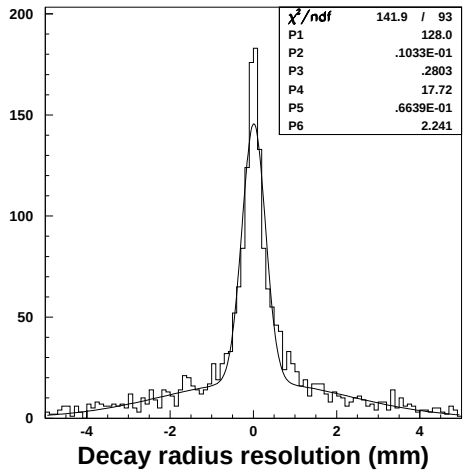

Fig. 9.55: Resolution of K^0_S decay radius.

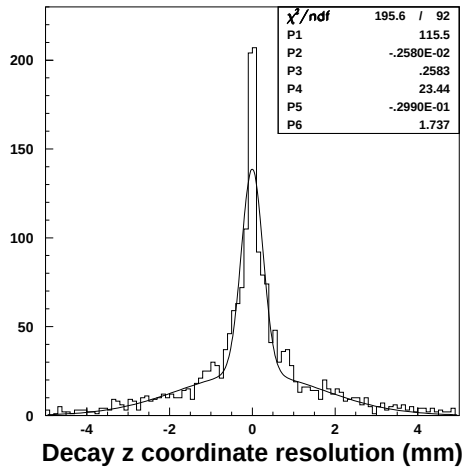

Fig. 9.56: Resolution of the K^0_S decay z position.

1. Global track reconstruction is performed using the CM algorithm with standard cuts. Tracks are required to have at least six hits with $\chi^2/\text{ndf} < 7$. An event is accepted for further analysis if there are at least 3 reconstructed muon tracks.

2. Secondary vertices are reconstructed using the GVF algorithm tuned for two-prong J/ψ and K^0_S vertices. The reconstructed J/ψ mass is required to be within a window of $\min(3\,\sigma, 70\ \text{MeV}/c^2)$ around the nominal J/ψ mass. The J/ψ vertex is required to be at least 2σ away from the beam axis. For K^0_S's, we use a mass window of $\min(3\,\sigma, 25\ \text{MeV}/c^2)$ and a transverse separation between the vertex and the beam axis of $\min(3\,\sigma,\ 1\ \text{cm})$.

3. We select a $J/\psi\ K^0_S$ pair which corresponds to a reconstructed mass inside a window of $70\ \text{MeV}/c^2$ around the nominal B^0_d mass value. We further require the reconstructed K^0_S to point to the measured J/ψ vertex and the reconstructed B^0_d mass to lie within $3\,\sigma$ around the nominal mass.

The global efficiency of this selection is 20%. The inefficiency is dominated by the K^0_S reconstruction. The efficiency to reconstruct 3 muons in an event is about 93%. Figure 9.57 shows the reconstructed mass distributions for the J/ψ and the $J/\psi\ K^0_S$ systems respectively. Gaussian fits to these mass distributions yield a resolution of $24\ \text{MeV}/c^2$ for J/ψ and $16\ \text{MeV}/c^2$ for B^0_d. The J/ψ mass resolution is about $16\ \text{MeV}/c^2$ when both muons are restricted to the barrel part of the Tracker.

Figure 9.58 illustrates the resolution of the reconstructed decay vertex of the B^0_d meson. Gaussian fits yield 40 μm resolution in the transverse plane and 74 μm resolution along the z direction.

Fig. 9.59 shows the resolution in proper time for the B^0_d decay. It corresponds to a resolution of 61 fs, estimated with a Gaussian fit to the distribution.

9.7 Heavy Flavour Identification

We use two different approaches to study the b-jet identification performance. The first method relies exclusively on the good accuracy of the track impact parameter measurement and is used

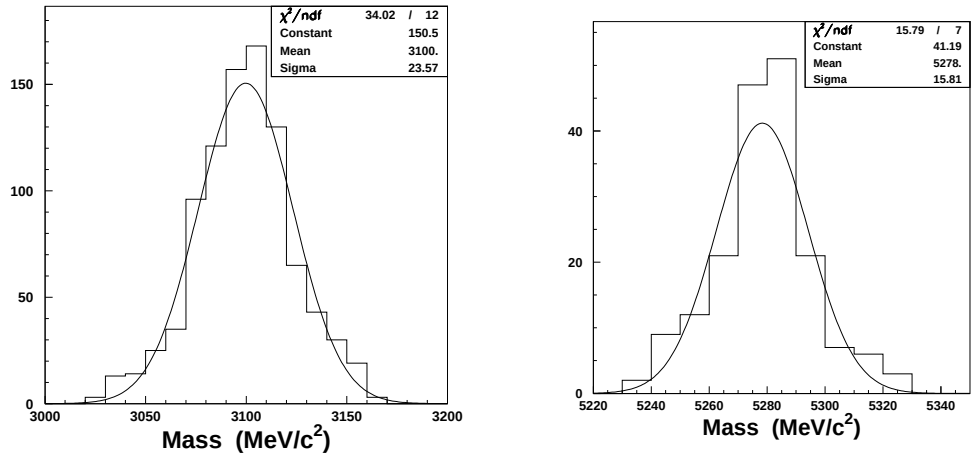

Fig. 9.57: Invariant mass of the reconstructed (a) J/ψ, (b) B_d^0 in $B_d^0 \to J/\psi K_S^0 \to \mu\mu\pi\pi$ decays.

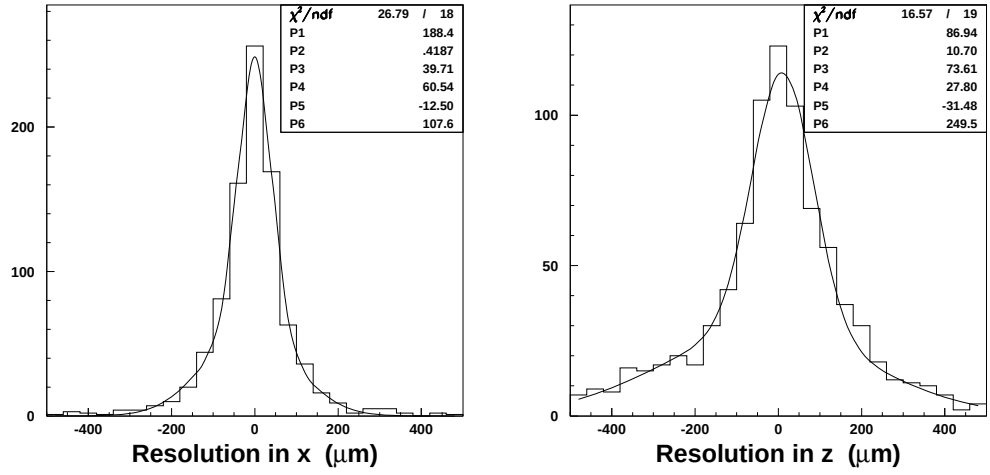

Fig. 9.58: Resolution of the reconstructed B_d^0 vertex along (a) x and (b) z axes. Gaussian fits to the cores yield 40 μm and 74 μm respectively.

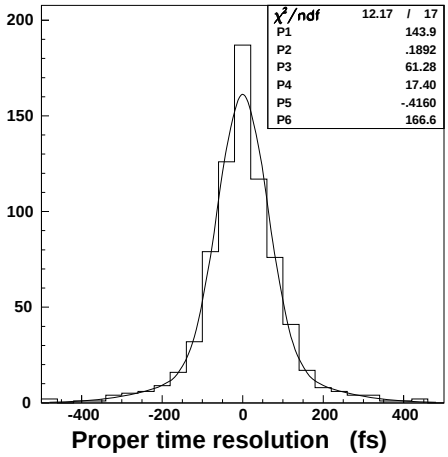

Fig. 9.59: Resolution of proper time for the B_d^0 vertex. A Gaussian fit to peak gives 61 fs.

to investigate the performance of the Phase I and II Tracker layouts. The second method relies instead on the identification of secondary vertices. To study b-jet identification we use the event samples described in Section 9.2.4.

9.7.1 Impact Parameter tagging

The $b\bar{b}$ and $u\bar{u}$ events are reconstructed using GTF, requiring at least 8 hits for track candidates. The tracks are required to lie within R=0.4 from the jet axis and to have $p_T \geq 1$ GeV/c, $d_0 \leq$ 2 mm and at least two hits in the Pixel detector. The sign of the transverse impact parameter is defined here by the sign of the projection of the impact point onto the jet axis, in the transverse plane. This definition of signed impact parameter $\vec{d_0}$ allows to neglect tracks with large impact parameter which are nevertheless 'uncorrelated' with the tracks clustered within the jet cones. A jet is considered tagged if at least N_{tr} of its tracks satisfy the condition that the signed impact parameter significance, $\vec{d_0}/\sigma_{\vec{d_0}}$, be larger than $N\sigma_{\vec{d_0}}$. Appropriate values for N_{tr} and $N\sigma_{\vec{d_0}}$ are 2 or 3, depending on the actual problem under study. Looser requirements improve b-tagging efficiency but also increase the probability to tag a non-b jet (mistagging rate). We show the b-jet tagging efficiency for jets of $E_T = 100$ GeV as a function of the mistagging rate in Figs. 9.60 and 9.61. In these figures, the b-tagging performance of the Phase I and II detectors is shown for three different η regions. At constant η the b-tagging efficiency and the mistag rate are evaluated for four of the possible requirements on N_{tr} and $N\sigma_{\vec{d_0}}$. The highest purity point is obtained by imposing the condition $N_{tr} = 3$ and $N\sigma_{\vec{d_0}}$=3, that we indicate here as $3_T \times 3_\sigma$. In increasing order of efficiency the conditions used are $3_T \times 2_\sigma$, $2_T \times 3_\sigma$, and $2_T \times 2_\sigma$. The b-tagging efficiency is highest for jets in the barrel Tracker. The efficiency drops by $\sim 10\%$ in the endcap region. On average, the mistagging rate varies within a factor two for jets at different pseudorapidities. The mistagging rate varies between 10^{-3} and 10^{-2} for the more stringent requirements $3_T \times 3_\sigma$

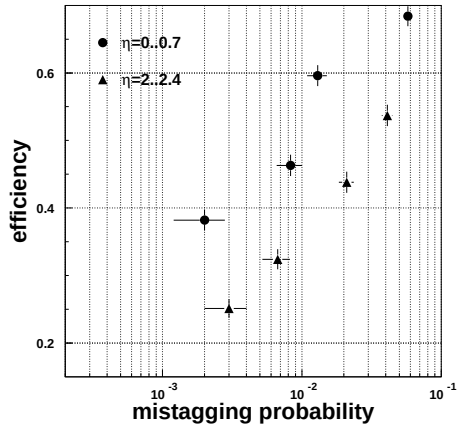

Fig. 9.60: b-tagging efficiency as a function of purity for 100 GeV E_T jets in two pseudorapidity intervals. Different tagging requirement are used and explained in the text. Phase I Tracker.

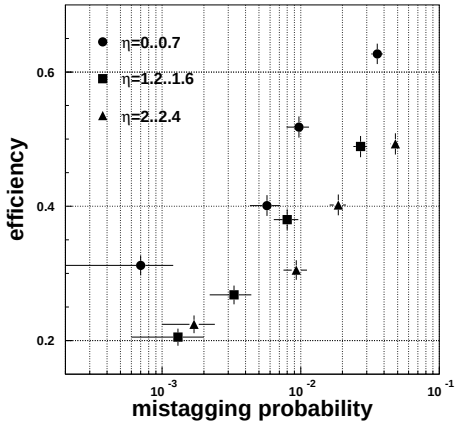

Fig. 9.61: b-tagging efficiency as a function of purity for 100 GeV E_T jets in three pseudorapidity intervals. Different tagging requirement are used and explained in the text. Phase II Tracker.

and $3_T \times 2_\sigma$. A more complete set of results is reported in Tables 9.8, 9.9 and 9.10. We have studied the tagging efficiency and the mistagging rates for jets in three pseudorapidity intervals and for three different values of the jet transverse energy. Each jet sample has been analysed by imposing the four different requirements on N_{tr} and $N\sigma_{\vec{d_0}}$ listed above. When the information is available, the performance of the Phase I Tracker is also shown in the tables. A study of the

tables shows that for equal tagging probability, the mistagging rate is slightly higher in jets of 50 GeV E_T than in the 100 GeV E_T jets. At higher jet E_T the purity decreases rapidly.

Table 9.8: B-tagging efficiency vs mistagging rate at $|\eta| < 0.7$, $p_t > 1$ GeV

	Phase I Tracker			Phase II Tracker		
$N_{tr} \times N\sigma_{\vec{d}_0}$	50 GeV	100 GeV	200 GeV	50 GeV	100 GeV	200 GeV
2×2	55.5 ± 1.6	64.7 ± 1.5	60.8 ± 1.5	48.4 ± 1.6	59.9 ± 1.6	59.1 ± 1.6
	1.40 ± 0.21	2.60 ± 0.29	6.00 ± 0.43	1.33 ± 0.21	2.40 ± 0.28	4.83 ± 0.39
2×3	46.1 ± 1.6	56.3 ± 1.6	52.9 ± 1.6	37.2 ± 1.5	48.9 ± 1.6	49.1 ± 1.6
	0.77 ± 0.16	0.77 ± 0.16	2.40 ± 0.28	0.53 ± 0.13	0.77 ± 0.16	1.73 ± 0.24
3×2	31.5 ± 1.5	44.0 ± 1.6	35.2 ± 1.5	27.0 ± 1.4	38.4 ± 1.5	34.6 ± 1.5
	0.30 ± 0.10	0.23 ± 0.09	1.17 ± 0.20	0.20 ± 0.08	0.33 ± 0.11	0.77 ± 0.16
3×3	23.5 ± 1.3	35.4 ± 1.5	28.0 ± 1.4	18.9 ± 1.2	28.8 ± 1.4	26.8 ± 1.4
	0.10 ± 0.06	0.10 ± 0.06	0.30 ± 0.10	0.07 ± 0.05	0.03 ± 0.03	0.17 ± 0.07

The Phase I Tracker has higher b-jet tagging efficiency since the barrel Pixel detector is closer to the beam pipe. The increase in efficiency for a given b-tagging requirement varies between 2% and 5% and it is in fact more remarkable in the two smaller pseudorapidity intervals considered in this study. The mistagging rates at equal tagging efficiency, are larger for the Phase II Tracker. In this study, standard GTF cuts have been used and no effort to tune the performance for b-tagging has been made. The mistagging rate can in fact be reduced and will be the object of further studies. We show a study of the b-tagging performance as a function of the p_T cut applied on the tracks used to tag the jets in Fig. 9.62a. For jets of $E_T = 100$ GeV in the barrel region of the Phase I Tracker, the tagging efficiency ($2_T \times 3_\sigma$) varies between 60%, for a cut of $p_T \geq 1$ GeV/c, and 37% if a cut $p_T \geq 5$ GeV/c is used ($3_T \times 3_\sigma$). In the same interval, the mistagging rate drops by a factor of 3. The dependence of the tagging efficiency and mistagging rate on the $\vec{d}_0$ significance is shown in Fig. 9.62b, using tracks of $p_T \geq 1$ GeV/c. The role of the Pixel detector in the b-tagging performance is high-lighted in Fig. 9.62c, which shows that at least two measurements in the Pixel detector are necessary to achieve high quality performance.

Table 9.9: B-tagging efficiency vs mistagging rate at $1.2 < |\eta| < 1.6$

	Phase II Tracker		
$N_{tr} \times N\sigma_{\vec{d}_0}$	50 GeV	100 GeV	200 GeV
2×2	39.0 ± 1.6	47.1 ± 1.6	53.6 ± 1.6
	0.90 ± 0.17	1.87 ± 0.25	4.17 ± 0.36
2×3	27.9 ± 1.4	35.8 ± 1.5	43.3 ± 1.6
	0.50 ± 0.13	0.73 ± 0.16	1.63 ± 0.23
3×2	17.9 ± 1.2	25.6 ± 1.4	29.3 ± 1.4
	0.12 ± 0.06	0.23 ± 0.09	0.43 ± 0.12
3×3	10.3 ± 1.0	18.4 ± 1.2	22.2 ± 1.3
	0.07 ± 0.05	0.13 ± 0.07	0.17 ± 0.07

9.7.2 B-tagging with 3D vertex reconstruction

The use of the vertex reconstruction for b-tagging is two-fold. As part of the vertex finding algorithms discussed in Chapter 8, all tracks are re-fitted to test explicitely for compatibility with anyone of the identified vertices. With this set of re-fitted tracks, one can improve the

Table 9.10: B-tagging efficiency vs mistagging rate at $2 < |\eta| < 2.4$

	Phase I Tracker			Phase II Tracker		
$N_{tr} \times N\sigma_{\bar{d}_0}$	50 GeV	100 GeV	200 GeV	50 GeV	100 GeV	200 GeV
2×2	42.4 ± 1.6	51.6 ± 1.6	53.7 ± 1.6	37.5 ± 1.5	46.9 ± 1.6	52.9 ± 1.6
	1.27 ± 0.20	3.17 ± 0.32	8.10 ± 0.50	1.37 ± 0.21	3.40 ± 0.33	7.07 ± 0.47
2×3	31.9 ± 1.5	42.0 ± 1.6	44.3 ± 1.6	27.3 ± 1.4	38.2 ± 1.5	42.9 ± 1.6
	0.67 ± 0.15	1.83 ± 0.24	4.80 ± 0.39	0.30 ± 0.10	1.40 ± 0.21	2.87 ± 0.30
3×2	22.5 ± 1.3	31.3 ± 1.5	30.6 ± 1.5	18.2 ± 1.2	29.6 ± 1.4	33.1 ± 1.5
	0.13 ± 0.07	0.47 ± 0.12	2.20 ± 0.27	0.10 ± 0.06	0.60 ± 0.14	1.47 ± 0.22
3×3	14.2 ± 1.1	23.6 ± 1.3	21.8 ± 1.3	11.3 ± 1.0	21.2 ± 1.3	24.4 ± 1.4
	0.07 ± 0.05	0.27 ± 0.09	$1.23pm0.20$	0	0.17 ± 0.07	0.67 ± 0.15

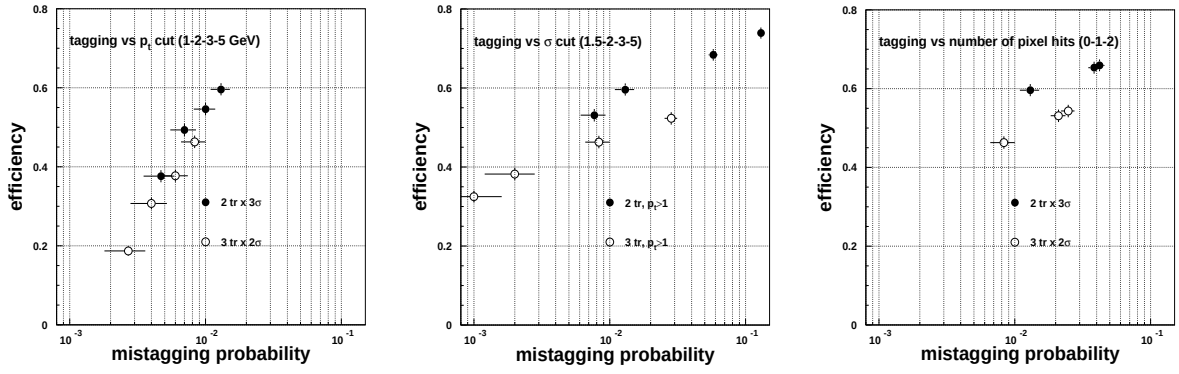

(a) **(b)** **(c)**

Fig. 9.62: Dependence of the b-tagging efficiency and mistagging rate on the a) p_T cut on the tracks within the jets, b) cut on the significance of the impact parameter and c) the number of track hits measured by the Pixel detector. Jets of E_T=100 GeV are used, generated in the barrel of the Phase I Tracker.

results of the conventional impact parameter tagging by removing the tracks associated with the primary vertices or two-prong decay vertices. This approach is referred to as Vertex Impact Parameter tagging (VIP). One can also directly use the reconstructed secondary vertices to tag b-jets (Secondary Vertex tagging, SV). Both approaches are considered for the barrel region of the Phase I Tracker detector, using the same jet event samples as above.

The track reconstruction is performed with the FKF track finder. The tracks with at least six hits, two of which measured in the Pixel detector, and $\chi^2/\mathrm{ndf} < 5$ are selected to identify b-jets. As one can see in Figs. 9.63 and 9.64 these cuts allow to control the reconstructed track quality to a good level even within the core of hard jets. The GVF vertex finder is used to reconstruct primary, secondary, K^0_S and Λ vertices. To suppress the mistagging rate, the GVF parameters were tuned to bias the algorithm to associate tracks with primary and two prong decay vertices.

For the VIP method, the impact parameter cuts are exactly the same as described in the previous section but, in addition, tracks are rejected if they are associated with some primary or V_0 vertex. An analysis of the mistagged jets is shown in Figs. 9.65 and 9.66 for jets of E_T = 100 GeV and E_T = 200 GeV in the barrel of the Tracker. After such cuts the relative mistagging rate due to tracks originating from the primary vertex is at the level of 20% (32%) and the mistagging rate due to K^0_S and Λ decays, is about 5%. The remaining fraction of $\sim$ 75% (64%) originates from the secondary interactions in the Tracker material.

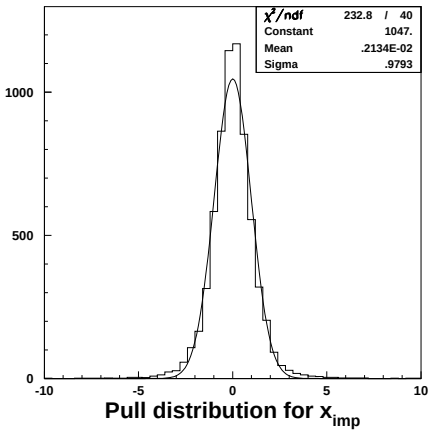

Fig. 9.63: Pull distribution of the x coordinate of the impact point (x_{imp}) for the reconstructed tracks with $p_T \geq 0.9$ GeV/c in the core of $E_t = 100$ GeV jet.

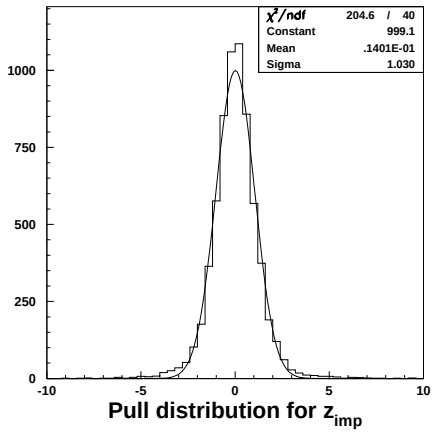

Fig. 9.64: Pull distribution of the z coordinate of the impact point (z_{imp}) for the reconstructed tracks with $p_T \geq 0.9$ GeV/c in the core of $E_t = 100$ GeV jet.

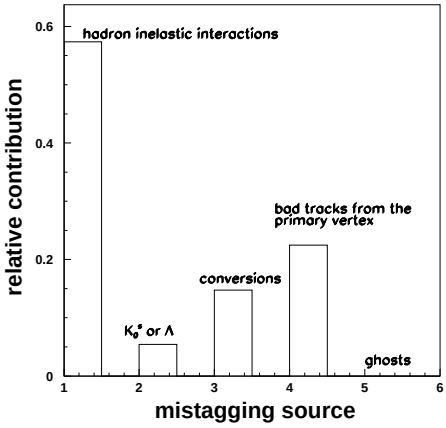

Fig. 9.65: Break-down of the mistagging rate in $u\bar{u}$ jets of $E_t = 100$ GeV. The fractional contribution to the mistagging rate is shown for tracks originated by different processes. All tracks satisfy the requirements $\bar{d}_0 \geq 3\sigma_{\bar{d}_0}$ and $p_T \geq 0.9$ GeV/c. Phase I Tracker layout.

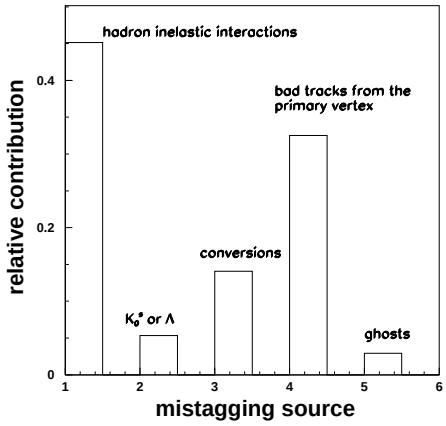

Fig. 9.66: Break-down of the mistagging rate in $u\bar{u}$ jets of $E_t = 200$ GeV. The fractional contribution to the mistagging rate is shown for tracks originated by different processes. All tracks satisfy the requirements $\bar{d}_0 \geq 3\sigma_{\bar{d}_0}$ and $p_T \geq 0.9$ GeV/c. Phase I Tracker layout.

In the SV-tagging method, we consider a jet SV-tagged if a secondary vertex is reconstructed using tracks that lie within R=0.4 from the jet axis. We impose a cut on the significance of the secondary vertex, requiring that the vertex radius be at least three times its error. An upper cut on the vertex radius is set at 3 cm.

To reduce the mistagging rate, two further constraints are tested, namely, 1) an implicit cut on the secondary vertex radial resolution ($\sigma \leq 500$ μm), and 2) the preselection of only tracks with significant impact parameter ($2\sigma_{\vec{d_0}}$) for the secondary vertex seeding (see Chapter 8). We refer to this study as 'SV+extra cuts'-tagging.

Finally, we applied the SV-tagging selection criteria to $u\bar{u}$ and $b\bar{b}$ events at the Monte Carlo level. The Monte Carlo level SV-tagging performance is evaluated in order to estimate the upper bound of its effectiveness and to test how much the present results differ from the best performance. In this case, all secondary vertices generated during the simulation phase are considered. A secondary vertex is selected for b-tagging if: 1) it has at least two 'reconstructible' associated tracks, i.e. tracks with $p_T \geq 0.9$ GeV/c and with at least six reconstructed hits, two of which measured by the Pixel detector; 2) the vertex transverse distance from the beam line is at least 100 μm and less than 3 cm; 3) it is not a K^0_S or Λ decay vertex. The results obtained with this method will be referred to as USV-tagging performance, and correspond to the performance achieved in the case of perfect pattern recognition capability and infinite vertex position resolution.

The b-tagging efficiency and mistagging rate for the four different methods are shown in Figs. 9.67 and 9.68 as a function of jet E_T. The comparison clearly shows the large potential of the SV-tagging method. The present SV algorithm based on the GVF vertex finder yields a sizable increase of b-tagging efficiency at the expense of some loss of purity, which nevertheless remains at the level of a few percent. The improvement is particularly remarkable for soft jets. In this case the purity can easily be maintained at values of $\sim 1\%$. This may be of importance for some physics processes such as the associated production of a light SM Higgs decaying to $b\bar{b}$ or the associated MSSM Higgs production ($gg \to h, H, A + b\bar{b}$ process for $\tan\beta \geq 5 - 7$). The comparison of SV-tagging results and SV + extra cuts-tagging results shows the large flexibility of the SV tagging method. Indeed, the mistagging probability is at the level or even better than for VIP-tagging algorithm. However, as one can see from the USV results, the present SV-tagging results are far from the best performance achievable. A more efficient and more robust vertex reconstruction algorithm, which is expected to improve the SV vertex tagging performance, is currently under study.

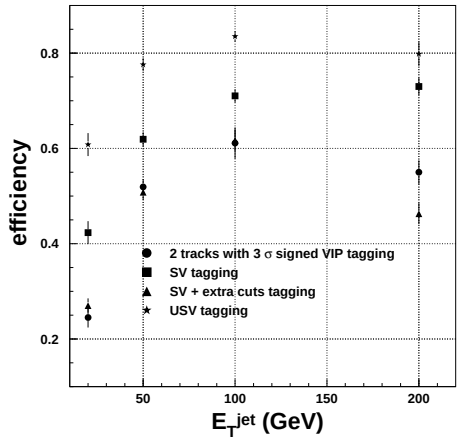

Fig. 9.67: b-tagging efficiency as a function of jet E_T, estimated using the four different approaches explained in the text.

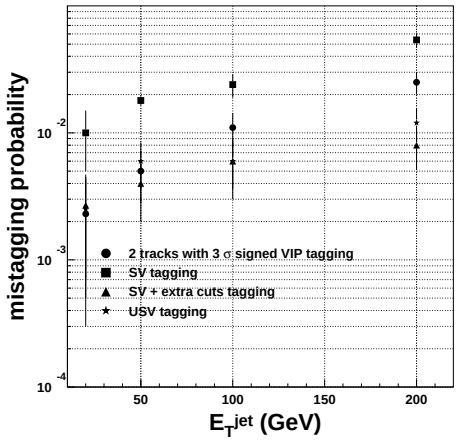

Fig. 9.68: Mistagging rate as a function of jet E_T, estimated using the four different approaches explained in the text.

We observe a sizable degradation of the b-tagging performance for $E_T = 200$ GeV jets. The loss of tagging purity is related with the diminished hit quality in the most precise Pixel and Silicon detectors, which is due to the large track density within the jet cores. The track fake rates or, in general, the fraction of badly reconstructed tracks increases, contributing to the mistagging probability. Moreover, the number of secondary interactions with the Tracker material increases by a factor of two with respect to the $E_T = 100$ GeV jets. However, even for $E_T = 200$ GeV jets b-tagging efficiency close to 50% and mistagging rates of $\sim 1\%$ can be obtained.

9.8 Heavy Ion Physics

9.8.1 Introduction

Heavy ion beams at the LHC will provide collision energy densities well above the threshold for the formation of QGP [9-3]. If such a new state of matter is created, all heavy quark bound states are allegedly suppressed by colour screening. Upsilon states can be detected through their decays to a pair of muons. The expected instantaneous luminosities are $\mathcal{L} = 10^{27}\mathrm{cm}^{-2}\mathrm{s}^{-1}$ and $\mathcal{L} = 2.5 \times 10^{29}\mathrm{cm}^{-2}\mathrm{s}^{-1}$ in the case of Pb and Ca ions, respectively. The design bunch crossing interval is 125 ns, and the expected total cross section in Pb-Pb collisions is 7.5 b, yielding a global event rate of 7.5 kHz. Trigger strategies have been analysed [9-2] that ensure high efficiency and good purity for muons originating from Υ decays. The expected global event rate is suppressed to 60 Hz by the di-muon trigger requirements. The signal events are collected at a rate of 10 Hz. They are predominantly Υ-induced with a smaller contribution from J/ψ or Z^0 di-muon decays. The task of the CMS Tracker is to recognise the muon tracks in an environment of tens of thousands of other tracks coming from the central ion-ion collision. In the most pessimistic scenario, the number of charged (neutral) particles produced in Pb-Pb collisions at $\sqrt{s} = 5.5$ TeV/NN can be as large as 8000 (4000) per unit of pseudorapidity. These particles are mainly low p_T (~ 0.5 GeV/c) pions or kaons. Consequently, the occupancies in the inner strip detectors ($r \leq 700$ mm) are rather large. Only those detectors which have a very high granularity (e.g. Pixel detectors) or which are positioned at large radii will have occupancies low enough to be useful in track finding.

Muons from Υ-decays have on average a transverse momentum of some 4 GeV/c. Though they lose nearly 2 GeV in the calorimeters and in the magnet coil, at least the innermost muon station [9-4] can be used in the pattern recognition process. The study presented here is restricted to the barrel detectors ($|\eta| < 0.8$). The reconstruction strategy employs the two Pixel layers, four outer layers of MSGC and two chamber planes of the innermost muon station.

In this analysis we use an earlier version of the Tracker layout where the strip length of all MSGC layers was 12.5 cm. In the current Tracker design, the two outermost MSGC layers are single ended, leading to a strip length of 25 cm. The increase in occupancy due to increased strip length in these MSGC layers has been estimated. The impact of the increased strip length on the reconstruction efficiency and mass resolution is presently under study.

9.8.2 Reconstruction method

Di-muons from Υ-decays are traced through the CMS detector using CMSIM. The main source of background to the di-muons are π/K decays that we have simulated separately. The signal and background samples are independently mixed with tracks from the underlying event due to the ion-ion collision. The underlying events are generated with varying multiplicity in the pseudo-rapidity interval $|\eta| < 5.0$, with a K/π ratio of 0.2 [9-5]. The shapes of η and p_T distributions are taken from the HIJING model [9-6] and the SHAKER [9-7] event generator, respectively.

The pattern recognition starts with one identified track segment in the innermost muon station. Clusters in the MSGC detectors are selected using a threshold on the signal per strip and a cut on the highest strip signal which depends on the number of strips in the cluster [9-8, 9-9]. Fig. 9.69 shows occupancy rates (ratio of number of fired strips to total number of strips per layer), with a threshold of 3500 e^- per strip, as a function of the radial position of the MSGC layer. The points are obtained from events generated with a rapidity density of 8000 charged particles.

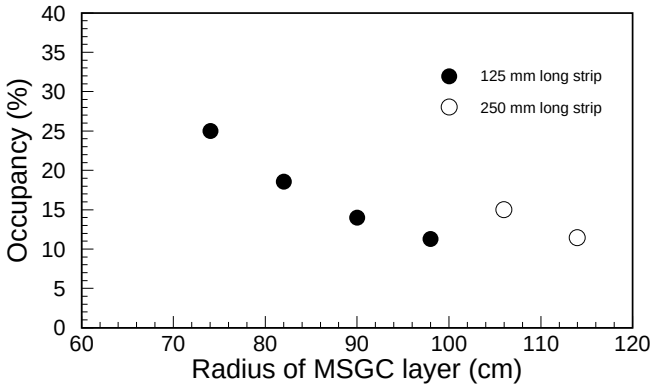

Fig. 9.69: Occupancy in MSGC layers for charged particle density $\frac{dN}{dy} = 8000$.

In the latest design of the Tracker the layers at 1067 and 1147 mm have strip lengths of 250 mm compared to 125 mm for the remaining layers. As can be seen from the figure, the occupancy stays well below 30% for all layers in the final design.

The seed for a track segment uses hits in the second chamber of the innermost muon station. The azimuthal angle, ϕ, is determined assuming the tracks to stem from the origin (0,0,0). The hits are matched with the next inner layer and the difference in ϕ of the two matched hits gives a first p_T estimate for the track candidate. These track candidates are propagated backward to the Tracker by defining a road and looking for a match in azimuthal angle ϕ and p_T. The estimates of ϕ and p_T are improved at each step. The highest level of ambiguity arises at the outermost layer of the Tracker where the predicted road is broadened by multiple scattering in the calorimeter. A road in θ starting from the two outermost MSGC layers is also used. A helix fit is performed through the selected points in the Tracker imposing a beam constraint. A linear fit is carried out in the rz-plane with the two additional muon chamber hits. The χ^2 values from the fits, combined with an estimator defined as:

$$\chi^2 = \sum_i \left(\frac{\phi_i^{predicted} - \phi_i^{measured}}{\sigma_i} \right)^2$$

are used to compute an overall quality parameter [9-8, 9-9] for the track candidate. The three track candidates with the best track quality parameters are preserved.

9.8.3 Identification of $\Upsilon \to \mu\mu$ events in AA interactions

Track pairs, reconstructed as above, are classified as like-sign or opposite-sign di-muons. The opposite-sign pairs are further constrained at the interaction point so that the separations along z and in the transverse plane are small:

$$\left(\frac{dz}{\sigma_z}\right)^2 < 6 \qquad \left(\frac{dr}{\sigma_r}\right)^2 < 14$$

with $\sigma_z = 50$ μm and $\sigma_r = 20$ μm . A quality criterion for each opposite-sign muon pair is defined as the product of the quality of each muon candidate and the vertex quality as:

$$K = \left[\left(\frac{dz}{\sigma_z} \right)^2 + \left(\frac{dr}{\sigma_r} \right)^2 \right]$$

The pair with the highest quality criterion is retained as an Υ candidate.

The mass of the reconstructed di-muon pair is shown in Fig. 9.70(a) for the Υ-decay sample. A narrow peak with a mass resolution of 47 MeV/c^2 can be seen. In contrast, the opposite-sign di-muons from π/K decays give a rather broad di-muon mass spectrum as shown by the solid histogram in Fig. 9.70(b). The dashed histogram in the same figure shows the mass spectrum for like-sign pairs from uncorrelated muons. The two mass spectra in Fig. 9.70(b) are similar except for a peak in the like-sign case at a di-muon mass of about $2m_\mu$ due to the selection of combinations including fake tracks.

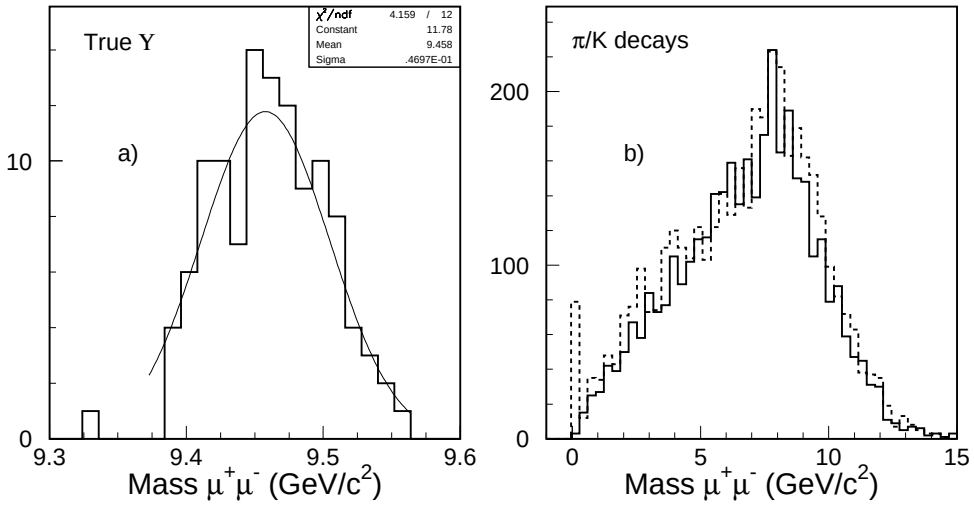

Fig. 9.70: Invariant mass spectrum of opposite-sign di-muon candidates for (a) signal Υ's, (b) uncorrelated background from π/K decays. The dashed histogram is due to like-sign di-muon candidates.

Assuming all MSGC strips to be 125 mm long and the charged particle density to be 8000, the di-muon reconstruction efficiency for Υ decays has been estimated to be 66% with 3% misidentification. A study has been made by dropping the layer at a radius of 1147 mm, keeping the layers at 827, 907, 987 and 1067 mm and choosing the strip length to be 250 mm for the two last layers. This study is more pessimistic than the low luminosity option, which has 125 mm long strips at the radii 827 and 907 mm as well as 250 mm strips at the radii 1067 and 1147 mm. One obtains an efficiency of 54% in this pessimistic scenario. However, the reconstruction efficiency can be improved by using the reconstructed z vertex position rather than the nominal beam position. It has been demonstrated that the z coordinate of the vertex can be determined with a precision of 130 μm using the Pixel detectors (see Fig. 9.71). With this additional information, the efficiency improves from 54% to 60%.

Table 9.11 summarises the reconstruction efficiency for opposite-sign di-muon pairs as a function of particle density. The efficiency decreases from 90% efficiency at low particle density to 66% for a charged particle density of 8000.

These reconstruction efficiencies and detector resolutions have been folded into the event generator information to obtain the di-muon mass spectrum. Fig. 9.72 shows the mass spectrum corresponding to one month's running of the CMS detector with Pb-ion beams. The background

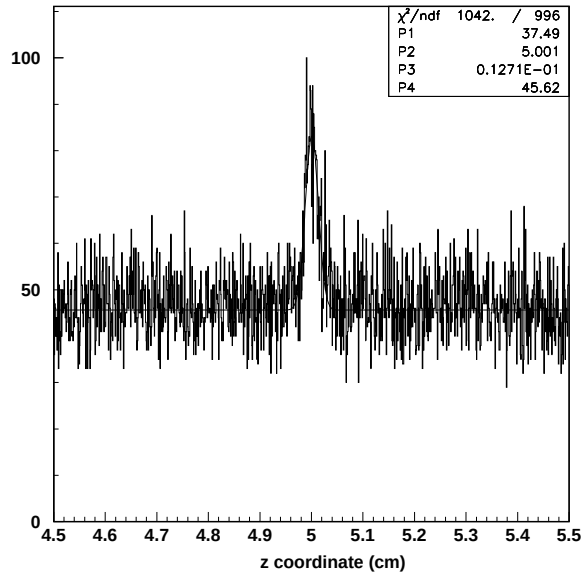

Fig. 9.71: z coordinate of reconstructed vertices using the measurements from the barrel Pixel layers with track density of 8000.

Table 9.11: Reconstruction efficiencies of muon-pair for different event multiplicity in samples where the di-muons come from Υ's, background due to π/K decays, or due to uncorrelated mixture of Υ, b-decays and π/K-decays

Source of μ's	Efficiency (%) for particle density of				
	500	1500	2500	5000	8000
Υ	88	90	88	83	66
π/K, π/K	7.9	7.6	7.8	7.5	5.6
Υ, π/K	19	19	19	18	14
Υ, b	36	35	34	33	25
π/K, b	15	15	14	14	11

subtraction is carried out using the like-sign di-muon mass spectrum. The signal to background ratio for Υ(1S) is 2 in Pb-Pb collisions increasing to 19 for Ca-Ca collision.

9.9 Summary of CMS Tracker Performance

The simulation and analysis of the CMS Tracker performance have been discussed in detail in Chapters 7, 8 and 9. Here we briefly summarise the main conclusions that can be drawn from this study.

As shown in Figs. 9.10 and 9.11, high p_T isolated tracks are reconstructed with a transverse momentum resolution of better than $\delta p_T/p_T \approx (15 \times p_T \oplus 0.5)\,\%$, with p_T in TeV/c, in the central region of $|\eta| \leq 1.6$, gradually degrading to $\delta p_T/p_T \approx (60 \times p_T \oplus 0.5)\,\%$, with p_T in TeV/c, as η approaches 2.5. This resolution is well suited to the reconstruction of narrow states decaying into charged particles, and is sufficient to ensure reliable charge assignment for muons and electrons up to the highest kinematically accessible momenta (Fig. 9.17).

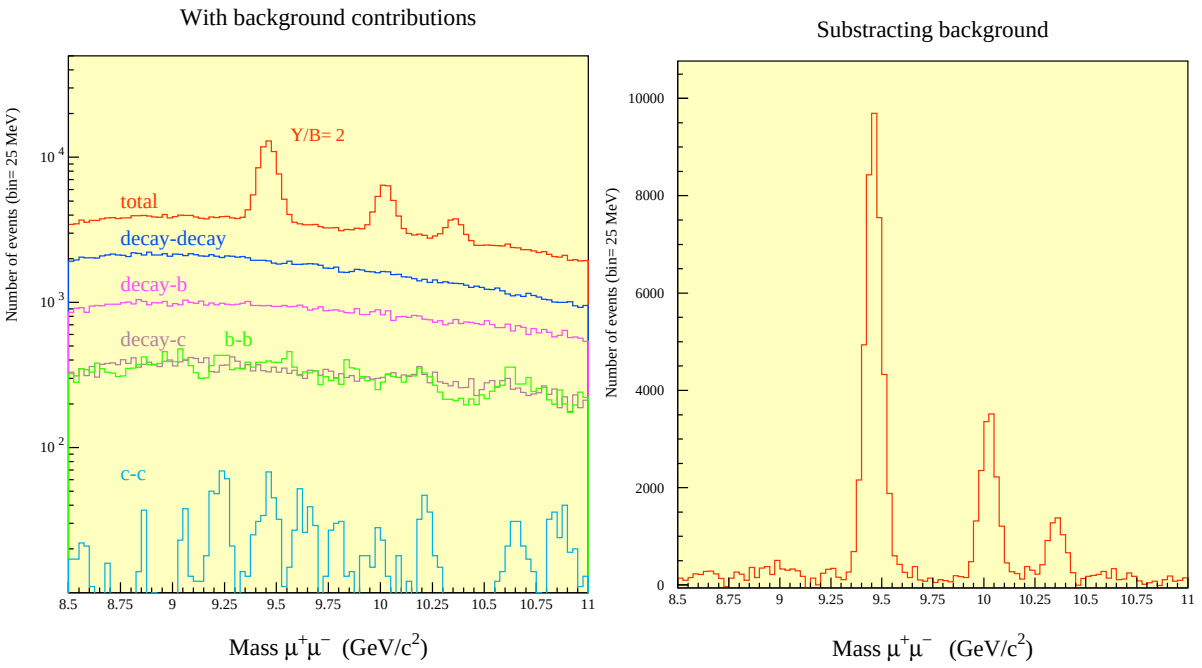

Fig. 9.72: Invariant mass spectrum of opposite-sign di-muon candidates as measured by the CMS detector from one month's running of the LHC with Pb-ion beams (a) without and (b) with background subtraction.

The reconstruction efficiency for muons is better than 98% over the full η range, even for values of p_T as low as 1 GeV/c (Fig 9.16, Fig. 9.23). High energy electrons are reconstructed with an efficiency above 90% (Table 9.3).

In the dense environment of a jet, charged hadrons with p_T above 10 GeV/c are reconstructed with an efficiency approaching 95%, and even hadrons with p_T as low as 1 GeV/c are reconstructed with an efficiency of better than 85% (Figs. 9.36 and 9.39). The highest efficiency is obtained with a pattern recognition algorithm (FKF) which, by taking the innermost layers of the Tracker as starting point and proceeding outwards, is able to efficiently and correctly reconstruct tracks even for a large fraction of those particles which interact inelastically before leaving the Tracker volume.

The impact parameter resolution in the plane perpendicular to the beams, shown in Fig. 9.6, is better than 35 μm over the full $|\eta| \leq 2.5$ range for particles with p_T above 10 GeV/c. The longitudinal impact parameter resolution, shown in Fig. 9.8, is significantly better than 75 μm over most of the rapidity range. At low luminosity it is possible to place the innermost Pixel layer closer to the beam line. This results in an appreciable improvement in impact parameter resolution, as can be seen from Figs. 9.5 and 9.7. Tails due to errors in track reconstruction are at a level well below the rate of displaced vertices due to long-lived particles (Figs. 9.37, 9.63 and 9.64).

In the central pseudorapidity region tagging efficiencies of 50% or better can be obtained for b jets ranging from 50 GeV to 200 GeV E_T, with a mistagging probability of about 1-2%. In the forward pseudorapidity region, for equal mistagging probability, the tagging efficiency remains around 40% (Figs. 9.60 and 9.61 and Tables 9.8 to 9.9).

The Phase I Tracker gives satisfactory performance in the low luminosity conditions, albeit with a noticeable loss of tracking efficiency within jets in the forward direction (Figs. 9.39 and 9.40). For the full Phase II detector, good tracking performance is achieved even within dense jets in the forward direction, and at high luminosity (Fig. 9.45).